C O M M U N I C A T I O N S

FACULTY OF SCIENCES
UNIVERSITY OF ANKARA

DE LA FACULTE DES SCIENCES
DE L'UNIVERSITE D'ANKARA

Series A2-A3: Physical Sciences and Engineering

VOLUME: 64 **Number: 1** **YEAR: 2022**

Faculy of Sciences, Ankara University
06100 Beşevler, Ankara –Turkey
ISSN 1303-6009 E-ISSN 2618-6462

C O M M U N I C A T I O N S

FACULTY OF SCIENCES
UNIVERSITY OF ANKARA

DE LA FACULTE DES SCIENCES
DE L'UNIVERSITE D'ANKARA

Series A2-A3: Physical Sciences and Engineering

Volume: 64 **Number: 1** **Year: 2022**

This Journal is published two issues in a year by the Faculty of Sciences, University of Ankara. Articles and any other material published in this journal represent the opinions of the author(s) and should not be construed to reflect the opinions of the Editor(s) and the Publisher(s).

Correspondence Address:
COMMUNICATIONS
EDITORIAL OFFICE
Ankara University, Faculty of Sciences,
06100 Beşevler, ANKARA – TURKEY
Tel: (90) 312-216 87 00 Fax: (90) 312-216 89 00
e-mail: commun@science.ankara.edu.tr
http://communications.science.ankara.edu.tr/index.php?series=A2A3

Print:
Ankara University Press
İncitaş Sokak No:10 06510 Beşevler
ANKARA – TURKEY

C O M M U N I C A T I O N S

FACULTY OF SCIENCES
UNIVERSITY OF ANKARA

DE LA FACULTE DES SCIENCES
DE L'UNIVERSITE D'ANKARA

Series A2-A3: Physical Sciences and Engineering

Volume: 64 **Number: 1** **Year: 2022**

Research Articles

Review Articles

http://communications.science.ankara.edu.tr

Commun.Fac.Sci.Univ.Ank.Ser. A2-A3
Volume 64, Number 1, Pages 1–20 (2022)
DOI:10.33769/aupse.1020175
ISSN 1303–6009 E-ISSN 2618–6462

Research Article; Received: November 07, 2021; Accepted: January 04, 2022

3D RECONSTRUCTION OF CORONARY ARTERIES USING DEEP NETWORKS FROM SYNTHETIC X-RAY ANGIOGRAM DATA

İbrahim ATLI[1] and O. Serdar GEDİK[1]

[1]Department of Computer Engineering, Ankara Yildirim Beyazit University, Ankara, TURKEY

Abstract. Cardiovascular disease (CVD) is one of the most common health problems that are responsible for one-third of all deaths around the globe. Although X-Ray angiography has deficiencies such as two-dimensional (2D) representation of three dimensional (3D) structures, vessel overlapping, noisy background, the existence of other tissues/organs in images, etc., it is used as the gold standard technique for the diagnosis and in some cases treatment of CVDs. To overcome the deficiencies, great efforts have been drawn on retrieval of actual 3D representation of coronary arterial tree from 2D X-ray angiograms. However, the proposed algorithms are based on analytical methods and enforce some constraints. With the evolution of deep neural networks, 3D reconstruction from images can be achieved effectively. In this study, we propose a new data structure for the representation of objects in a tubular shape for 3D reconstruction of arteries using deep learning. Moreover, we propose a method to generate synthetic coronaries from data of real subjects. Then, we validate tubular shape representation using 3 typical deep learning architectures with synthetic X-ray data we produced. The input to deep learning architectures is multi-view segmented X-Ray images and the output is the structured tubular representation. We compare results qualitatively in terms of visual appearance and quantitatively in terms of Chamfer Distance and Mean Squared Error. The results demonstrate that tubular representation has promising performance in 3D reconstruction of coronaries. We observe that convolutional neural network (CNN) based architectures yield better 3D reconstruction performance with 9.9e-3 on Chamfer Distance. On the other hand, LSTM-based network fails to learn the coronary tree structure and we conclude that LSTMs are not appropriate for auto-regression problems as depicted in this study.

Keywords. 3D Reconstruction, coronary artery tree, deep learning, synthetic coronary dataset.

iatli@ybu.edu.tr-Corresponding author; gedik@ybu.edu.tr
0000-0003-0393-2332; 0000-0002-1863-8614.

1. INTRODUCTION

Cardiovascular disease (CVD) is one of the serious health problems which may lead to death if not treated appropriately. According to the research conducted by World Health Organization (WHO), it is reported that an estimated 17.9 million people die (31% of all deaths worldwide) each year from CVDs [1]. Precise diagnosis and treatment have the potential to increase the quality of life of patients and decrease the rate of deaths. There exist many imaging methods utilized for the diagnosis of CVDs such as Magnetic Resonance Imaging (MRI), Digital Subtraction Angiography (DSA), Computed Tomography Angiography (CTA) and XRay Angiography (XRA). Among them XRA imaging modality is a gold standard technique used in clinics [2, 3]. However, XRA provides 2-dimensional (2D) images to monitor blockages, aneurysms, narrowing, malformations and other blood vessel problems in veins, arteries and organs in screens. Interventional cardiologists capture images from different views of angle [4] and examine these images to make a diagnosis. They decide on treatment planning by investigating the anatomical features of arteries. In some cases, it is possible to treat blocked vessels during the angiogram, but further examination is recommended after surgery to diagnose a variety of vascular problems including aneurysm, vascular malformations, deep vein thrombosis, aortic arc (problems in the arteries that branch off the aorta), peripheral artery disease and renovascular conditions [5]. These tasks are not trivial due to the following factors: (1) The images are generally in low quality and contrast; (2) XRA imaging is limited by inherent 2D representation of 3D structures. It creates 2D projection images and the projection operation causes a substantial amount of 3D/4D anatomy information of the coronary artery to be lost. (3) Cardiologists need to combine all images mentally in their minds to resolve the problem and its location; (4) the accurate diagnosis heavily relies on the experience of cardiologists, and (5) this creates a subjective evaluation; (6) Finally, the procedure of X-Ray imaging is not convenient to be repeated multiple times because it needs surgical intervention and injection of contrast (radioactive) material directly to arteries. Although tackling these problems manually is possible, it takes hours of processing and evaluation for each patient. It is a cumbersome, repetitive and operator-dependent task. Decreasing intra or inter-operator variability and improving the quality of diagnosis in terms of time and accuracy is possible with an automated tool. In this manner, a system generating 3D model of heart vessels can provide objective, reproducible and relatively easier evaluation. Such a system offers a new and accurate approach in diagnosis and has the potential to guide clinical decisions. Therefore, the development of automatic and accurate vessel-tree reconstruction from angiograms is highly desirable. The aim of this study is to develop a fast, robust and automated deep-learning (DL) tool for 3D reconstruction of coronary artery tree from X-Ray angiograms to provide clinical assistance.

3D reconstruction with deep learning methods is a topic of high interest and researchers improve algorithms and data structures as the number of 3D data-sets

increases. We identify that previous works have only focused on analytical solutions for 3D reconstruction of coronary arteries as reviewed in Section 2. Although 3D reconstruction can be achieved effectively using deep learning, there is no 2D or 3D publicly available coronary artery data-set in literature. In this paper, we present a synthetic 3D data-set (5000 left, 5000 right coronary artery) and make following contributions:

- We propose a novel data structure for the representation of 3D tubular shapes.
- We have validated that our data structure works well in 3D reconstruction of coronaries using 3 basic deep networks both qualitatively and quantitatively.
- We introduce a method to generate synthetic 3D coronaries from 3D computerized tomography data of real subjects,
- We show deep networks can be utilized in 3D reconstruction of coronaries. This is the first study that uses DL in 3D reconstruction of coronaries,
- We demonstrate that long-short-term-memory (LSTM) is not a proper choice for auto-regression problems as in [6],
- The proposed method has the potential to be used in clinics due to its decent running-time.

The rest of the paper is organized as follows: Section 2 presents related work. Section 3 introduces the materials and proposed method. In Section 4, experimental results are presented. Finally, we draw our conclusions, discuss the limitation of the work and mention future directions in Section 5.

2. Related work

There are various 3D coronary reconstruction methods that stem from different types of coronary imaging systems. The studies presented in [3, 7–13] utilize traditional (single-plane) XRA and [14–18] utilize biplane XRA. We focus on these XRA methods and examine them into 2 main categories based on the technique they follow: (1) Calibrated and (2) non-calibrated (calibration-free) reconstruction. Then, we continue to present learning based methods specifically. Since 3D reconstruction of coronary arterial tree with DL has not been addressed in the literature, we review DL-based methods for only 3D object reconstruction. We present them in groups according to the 3D representation they use.

In calibrated methods, camera calibration matrix is formed in order to map points in 3D to their corresponding 2D projections. Calibration parameters are estimated by optimizers [3,9–11] or using the phantom object on which metal balls are attached [19]. Centerlines [7–9, 14] or corresponding 2D points [3, 11] are used in determining calibration parameters and estimating 3D model of coronary artery tree. [3] and [9] follow the same approach in finding external parameters of the camera (R: rotation, t: translation) using constrained nonlinear optimization algorithm

given five or more correspondence points. The works [9–11,16] use epipolar matching and triangulation methods during 3D reconstruction of coronaries after calibration. Apart from these studies, [18] utilizes bundle adjustment method and [13,20] utilize graph-cut based sparse stereo method for 3D reconstruction. The works of [7,8] use deformable model and update contours using active contour algorithms with back-projection external energy. Similarly, [3] proposes active contour model and [14] uses Fourier deformable model with projective external energy. Although most of the studies assume heart is rigid during 3D reconstruction, [3, 13, 14, 17] include motion caused by respiration and heartbeat into their methods and obtain 4D model of coronary artery tree. In [8,10,11,13,15], X-ray images are synchronized using electrocardiography (ECG) recordings to ease 3D reconstruction process.

Calibration-free solution of [18] utilizes Random Sample Consensus (RANSAC) [21] method and eight-point algorithm to estimate the fundamental matrix for 3D reconstruction. In this way, the method internally achieves self-calibration in XRA image sequences. RANSAC method produces reliable correspondences during matching of centerline points. The work of [12] does not require calibration and uses a non-linear optimization algorithm to estimate projection matrix directly by making some assumptions on rotation of C-arm. The method tries to minimize the error between centerline points and back-projection of 3D reconstructed points.

It is clearly seen that classical 3D reconstruction methods depend on mathematical derivations between 2D and 3D geometry using some assumptions (pin-hole camera model). This process requires camera parameters to be known or estimated. For the ill-posed situations, where camera parameters are not known, feature correspondences are utilized to achieve self-calibration [18]. However, recent 3D reconstruction literature shows that objects can be reconstructed without calibration by the utilization of deep learning methods. Tremendous amount of progress has been drawn in last 5 years in learning-based 3D reconstruction. The problem remains challenging because there is not enough 3D data for training and there are many ways to represent 3D models such as point clouds, meshes, volumetric grids (voxels), etc. The proposed methods change according to the representations of 3D models. Moreover, although DL based methods are not utilized in the 3D reconstruction of arteries, in this part we focus on DL based object reconstruction methods. Thus, we divide 3D object reconstruction literature into 4 main categories based on their 3D representations as following: (1) point-cloud [22–26], (2) volumetric grids [27–34], (3) polygonal mesh [35,36], (4) other specific data structures [25,37,38].

Point cloud representation is one of the most popular object representation techniques in computer graphics and computer vision. Data is simple to read, write and interpret in this format. However, the number of points should be limited if this format is used in deep learning architectures due to pre-determined output size. CAPNet is introduced in [22] and method uses an encoder-decoder architecture to obtain point cloud reconstructions from 2D image(s). Arbitrary views of reconstructed point clouds are projected onto 2D plane to refine point clouds with

known camera parameters. Fan et al. [23] propose a network, PointOutNet, for generating 3D objects from a single image by obtaining its own conditional shape sampler. The output shape is 1024x3 in PointOutNet. Zamorski et al. [24] propose adversarial auto-encoders to learn 3D latent space of compact representation of 3D point clouds and generate 3D shape out of it. In [25], a deep learning method is proposed for reconstructing 3D shapes from 2D sketches in the form of line drawings. The network produces depth and normal map of input sketches and these outputs are transformed into a dense point cloud representing a 3D reconstruction of the input sketch. In [26], neural networks are trained to produce corresponding depth maps and silhouettes from input images. From these silhouettes and depth maps 3D point cloud is generated and refined.

Volumetric grid representation is generally preferred in the related literature because outputs of deep learning architectures are definite in terms of size. In this method, objects are placed into a 3D grid and grid size is constant. In [27], a recurrent network based solution is proposed for 3D object reconstruction from single or multi-view images. The architecture, called 3D-R2N2, takes a 127x127 input image and generates features from that image using auto-encoder network. The output of auto-encoder network is fed into gated recurrent unit (GRU) based recurrent network to hold necessary features in its internal memory. Finally, 3D reconstruction of arbitrary viewpoints of images is achieved in 3D occupancy grid (32x32x32 voxel grid) with a decoder network. Training and testing are achieved using ShapeNet [39], PASCAL VOC 2012 [40] and online 3D databases. In [32], an enhanced version of 3D-R2N2 is proposed by changing regular voxel values into weighted representation. In weighted representation, voxels are defined as integer in the range of (-53, +53) instead of 0 and 1. Neighbor voxels are taken into account with 3x3x3 kernel filter in their representation. It is claimed that training time is also improved in this way [32]. [28] and [29] propose deep learning architecture using Octree [135] structure for obtaining higher resolution of a 3D model in grid voxel representation. By using Octree, 3D models can be generated efficiently in terms of memory and calculation because the architecture does not have cubic complexity for 3D object (for instance:256*256*256 or 512*512*512). The neural network learns Octree structure in [29]. Wang et al. [31] design O-CNN, a novel octree data structure, to efficiently store the octant information occupied by 3D surfaces. The surface of objects are predicted at different scale of voxel blocks with octrees in [33] by using an encoder-decoder network. In order to incorporate the physics formations such as perspective geometry and occlusion, Markov Random Fields with ray-potentials are explicitly modeled with CNN in [34]. Yan et al. propose an encoder-decoder network for 3D object reconstruction (output size 32*32*32) without 3D supervision by including perspective projection in the loss function [30]. In this study, the intrinsic and extrinsic parameters are known for the camera.

Polygonal mesh representation is another format used mostly in computer graphics, games and animations. Wang et al. [35] generate meshes by deforming an ellipsoid into the desired shape from a single color image using convolutional neural network (CNN). Distance between camera and objects are assumed to be fixed. Pontes et al. [36] find the similar objects in the image from the 3D database using classification index and deform this object with the parameters that are produced using neural network. The method can reconstruct 3D shape of the object from single image. We include other 3D representations into problem specific part because these are mostly data-specific formats. For instance, [37] utilizes encoder-decoder architecture for constructing RGB+D of a given single image view of a car or a chair. Point cloud and mesh are generated from multi-view RGB+D output of the network. They train their network with ShapeNet [39]. Lun et al. [25] propose a deep learning method for automatically translating hand-drawn sketches into 2D images representing surface depth and normal across several output views. Encoder-decoder network is utilized for generation of 12 normal maps and corresponding depths. 3D point cloud and polygonal mesh of object are obtained by fusing these depth and normal predictions later. A relatively new study presented in [38], introduces 3D representation of an object with defining 64D vector. The vector makes a 3D object predictable from 2D images.

3. Material and Methods

Three-dimensional reconstruction itself is a challenging problem due to various requirements and constraints. The algorithms proposed in the literature follow similar analytical methods like finding correspondences between images, estimating camera parameters, using epipolar constraints, etc. as mentioned earlier in Section 2. There are many parameters in analytical solutions. On the other hand, deep learning architectures with appropriate data structures can eliminate the parameters that analytical methods use.

In this study, we propose a simple data structure for tubular shaped objects and validate this representation in reconstruction of coronaries. To the best of our knowledge, this is the first study that employs deep learning in the reconstruction of coronary arteries. Moreover, we present a method to generate a synthetic data-set and make it publicly available for researchers. This section presents details of synthetic data-set generation and proposed data structure along with some simple deep networks.

3.1. **Synthetic 3D Data Generation.**

Deep network architectures require plenty of labeled training data in order to learn input and output relationships. If the number of elements in the training set is lower, the network memorizes input-output relation, called overfitting. In this case, the network performance (the quality of output) degrades in tests. To generalize network for better test results, training should be accomplished using a relatively large data-set. Thus, we randomly generate 10000 3D models from real coronaries of nine subjects from [41]. We also

generate centerlines and corresponding radius in order to use them in the proposed method.

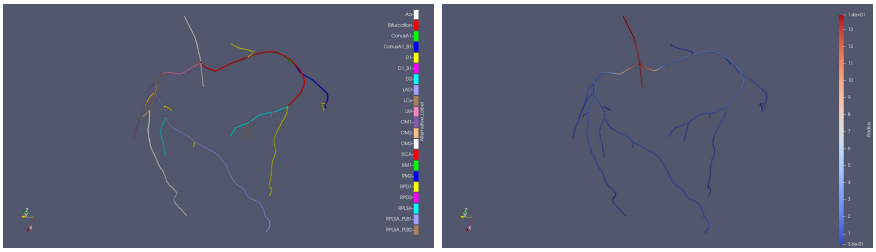

FIGURE 1. Coronary arteries of one of the subject in [41]. Branches are shown on the left and corresponding radii are shown on the right. The units are in mm for radii.

Left coronary artery (LCA) and right coronary artery (RCA) are branched off from the aorta to supply blood to the different parts of heart muscles. White colors on the left in Fig. 1 show aorta (Ao), red colors show main RCA branch and pink colors show the start of LCA. Typically, X-Ray angiogram is applied to one side of the arterial tree. Thus, we separate LCA and RCA branches during generation of synthetic data-set. In this way, networks can specifically learn anatomical properties of LCA and RCA structures. Another advantage of separating main branches is that the output size of the network becomes smaller. This will yield less computation and faster prediction time. Later, the combined version of the arterial tree can also be produced using the same logic presented here.

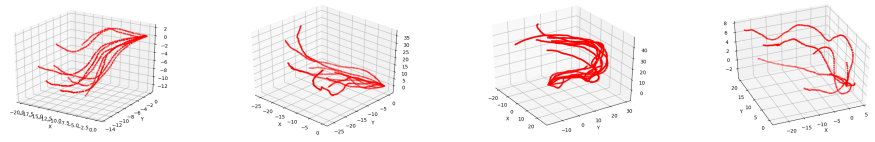

(A) (B) (C) (D)

FIGURE 2. Some of the branching patterns of coronary arterial tree. (A) and (B) branches of left main (LM) and left circumflex (LCx) arteries on LCA. (C) and (D) are RCA and the acute marginal branch (M1) on RCA.

We do not utilize the actual 3D data (centerline and radius) from [41]. We create random vessel trees by selecting one of the corresponding branches from 9 subjects. Additionally, some of the branches follow a similar path and we add them to the same group to obtain a random pool. We determine similarities by looking at visually multiple samples of branches. Vessels with similar patterns are gathered into the same group. In this way, we increase the variety of coronary trees that can

be encountered in real cases. Example branching patterns for some of LCA and RCA branches from 9 subjects can be examined in Fig. 2.

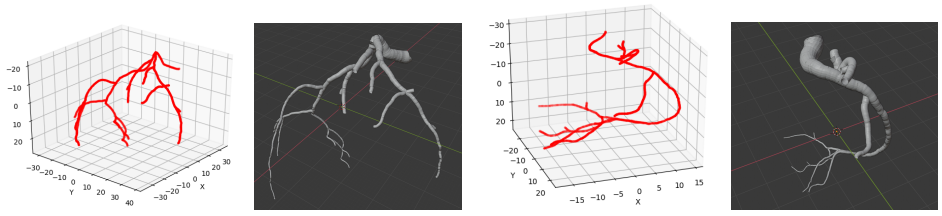

(A) (B) (C) (D)

FIGURE 3. The coronary trees synthetically produced from our method. (A) shows 3D centerline points of (B) for LCA. (C) shows 3D centerline points of (D) for RCA.

We introduce more randomization to the vessel generation procedure to expand diversity of coronaries. There is a possibility to deviate 3D coordinates of centerline points and their corresponding radii. Some branches are also determined to be added in the coronary tree with an 80% possibility from the related random pool. We also add the possibility to change the distance between two consecutive centerline points. In this way, we can produce various coronary vessel forms that may resemble real coronary trees. It is a very low possibility to generate the same vessel tree in this configuration. Some example outputs from vessel generating software are illustrated in Fig. 3 with their 3D centerlines.

In order to obtain 3D model of coronaries, we perform a sampling operation around the center and corresponding radii. Since this process requires vector operations in 3D space, we provide implementation details of tubular shaped representation and its transformation into 3D objects in Appendix A. Once the 3D coronary is obtained, 2D images of the model should be produced from different views. Simulating C-arm machine behavior to generate images similar to X-Ray angiograms is described in detail in Appendix B.

3.2. **Proposed Networks.** We propose 3 deep learning-based architectures for 3D reconstruction: (1) Multi-view fully CNN, (2) Time distributed auto-encoder CNN and (3) Auto-encoder followed by LSTM. The input to the networks is multi-view coronary vessel tree and the output is the sequential data structure we proposed for tubular shapes (see details in Appendix A).

3.2.1. *Multi-view CNN.* We propose fully CNN network as shown in Fig. 4 for the construction of 3D synthetic coronaries. In this architecture, multi-view images are provided to the network as channels. Thus, we name it as Multi-view Fully CNN (MvFCNN). We add residual connections to carry features from previous layers to deeper layers. This approach generally prevents loss of information and performs better performance on the given task. The convolution filter size for each layer for

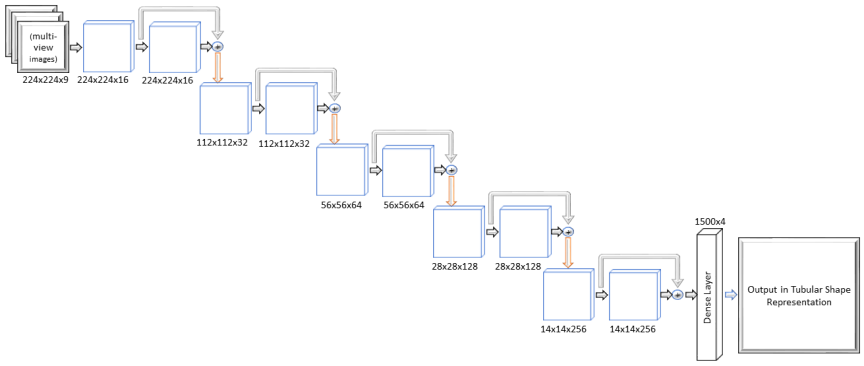

FIGURE 4. Multi-view fully CNN 3D reconstruction network. Activation function followed by each 3x3 convolution layer is Leaky-ReLU. Gray and orange arrows show residual connections and down-sampling with strided convolution (s=2), respectively.

MvFCNN architecture is 3x3. Downsampling is achieved using convolution operation with a stride of 2. In this way, the architecture continues to update weights while shrinking the size of the input (or embedding information from inputs) in intermediate layers. We utilize residual connections to transfer hierarchical representations to deeper layers of the network. In the end, we utilize fully connected layer to transform embedded information into the data structure we defined for the tubular shapes. Finally, we convert tubular shape representation into 3D objects using some math described in A.

3.2.2. *Time-distributed Auto-encoder CNN.* We use the same MvFCNN architecture of the previous section, but modify input and output layers to build a larger network as shown in Fig. 5. The differences are that (1) input images are separately supplied to the network instead of giving them as channels and (2) we remove the fully-connected layer at the end. In this way, each image is encoded into a feature space with the same auto-encoder. The features coming from different images are combined and used to produce our structured output with fully-connected layer. Fig. 5 visualizes this process clearly. In this figure, images of the same coronary tree are denoted as $X_1, X_2, \ldots, X_n$. These images are supplied to the same network to produce corresponding embedded features $E_1, E_2, \ldots, E_n$. Finally, embedded features are fed into a dense layer to produce our structured output.

For simplicity, we abbreviate time-distributed auto-encoder network as "TDAEn-Dense". In this naming convention, TD stands for time-distributed, AEn stands for auto-encoder and Dense is the final layer.

3.2.3. *Auto-encoder LSTM Decoder.* We use an auto-encoder network to embed features into a latent-space, and pass these features into memory cells of LSTM to hold necessary information that is coming from the current input. We remove the

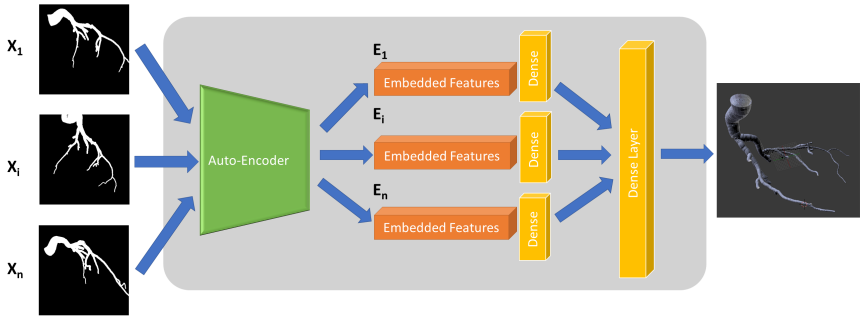

FIGURE 5. Time-distributed auto-encoder network. Input images are provided to the network in series.

fully connected part of the network in Fig. 5 and replace it with LSTM. In order to extract embedded information in LSTM cells, we place a decoder network at the end of LSTM. In this configuration, LSTM learns to hold important features in its internal memory and updates its hidden state according to incoming inputs. The network is abbreviated as En-LSTM-Dec in this study. The LSTM cell size is set to 1500.

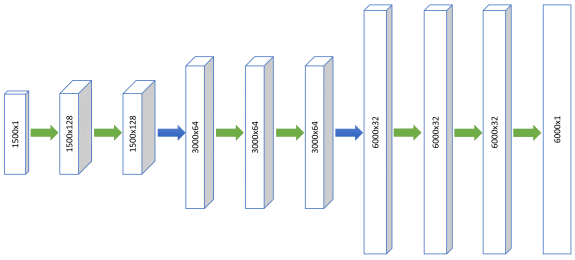

FIGURE 6. The decoder part for 3D reconstruction network.

The decoder part plays an important role in the architecture because the entire input sequence is now represented in LSTM's memory cells as a fixed-length vector. This encoded vector should be transformed into desired output sequences. The intuition here is that the decoder learns this complex representation and extracts the embedded information that LSTM holds. Thus, the output of LSTM is provided to the input of the decoder part in Fig. 6 to decode the embedded information within it.

3.3. **Performance Measures.** We evaluate the performance of 3D reconstruction predictions for 3D deep network architectures using Chamfer Distance (CD). It is utilized in ShapeNet's [39] shape reconstruction challenge. However, this measure

works with point cloud representation. Therefore, we use center points in our structured data definition of 3D tubular objects for quantitative comparisons. CD is the evaluation criterion for estimating 3D points in our data representation. However; our networks also predict the radius of each point. To compare network performance quantitatively, we use mean squared error (MSE) to evaluate average error on the radius as follows:

$$E_R(r, \widetilde{r}) = \frac{1}{M}\frac{1}{N}\sum_{s}\sum_{i}(r_{si} - \widetilde{r_{si}})^2 \tag{1}$$

where M is the number of test samples, N is the number of points in sample s, r_{si} and $\widetilde{r_{si}}$ are the reference (ground-truth) and predicted radius values in test sample s for the point at i.

4. Experimental Results

In this section, we show the validation of our 3D reconstruction methods using synthetic data-set we produced from real subjects as mentioned earlier in Section 3.1. We share the results of several experiments conducted on networks and compare their reconstruction performances in terms of CD and MSE. We present network comparisons under three subsections. The first section compares predictions quantitatively using statistical measures. The second section compares them qualitatively and finally, the last section compares the average running time.

4.1. Quantitative Comparison for 3D Reconstruction.

We quantify the performance of each network proposed for multi-view 3D reconstruction of coronary arteries and report the results in terms of CD and MSE. CD is used for the evaluation of center-line points in 3D and MSE is used for the evaluation of radius estimations. The lower values of both metrics indicate better 3D reconstruction that networks estimate.

There are 3 different 3D reconstruction networks described in Section 3.2. Table 1 shows the results of each network. In order to show network comparisons fairly and clearly, we present results with statistical measures; namely, mean (μ) and standard deviation (σ).

Table 1. Reconstruction performances of networks proposed in this study.

Model Name	**Chamfer Distance**		**Radius Error**	
	μ	σ	μ	σ
MvFCNN	0.00998328	0.00299526	0.00000580	0.00000226
TDAEn_Dense	0.03288964	0.02404985	0.00014654	0.00039439
En_LSTM_Dec	1.54436864	0.17509677	0.29157797	0.15928418

As shown in Table 1, MvFCNN outperforms others. The second architecture which achieves relatively good performance is TDAEn_Dense. These two architectures have no memory structure and data is provided explicitly as part of their

input. However; in LSTM-based architecture, data is provided in series and it is expected to remember past observations. We observe that the architecture with internal memory (LSTM) have the largest errors in both metrics. The reasons why LSTM-based network performs poorly on 3D reconstruction might be that (1) the number of epoch or (2) memory units are not enough (it was 500 epoch and 1500 memory unit for LSTM in this study) for them to learn hidden representations or (3) they are not suited for auto-regression type problems as stated in [6]. Increasing the number of training epochs or using a stack of LSTMs may have improved the results but the network sizes are quite large as in the current configuration. Prediction time increases as the number of parameters are increased. Thus, we do not add more layers to memory-based network. We perform an additional test by increasing the number of units in LSTMs to 3000, but it does not improve the reconstruction performance for at least learning the vessel tree structure.

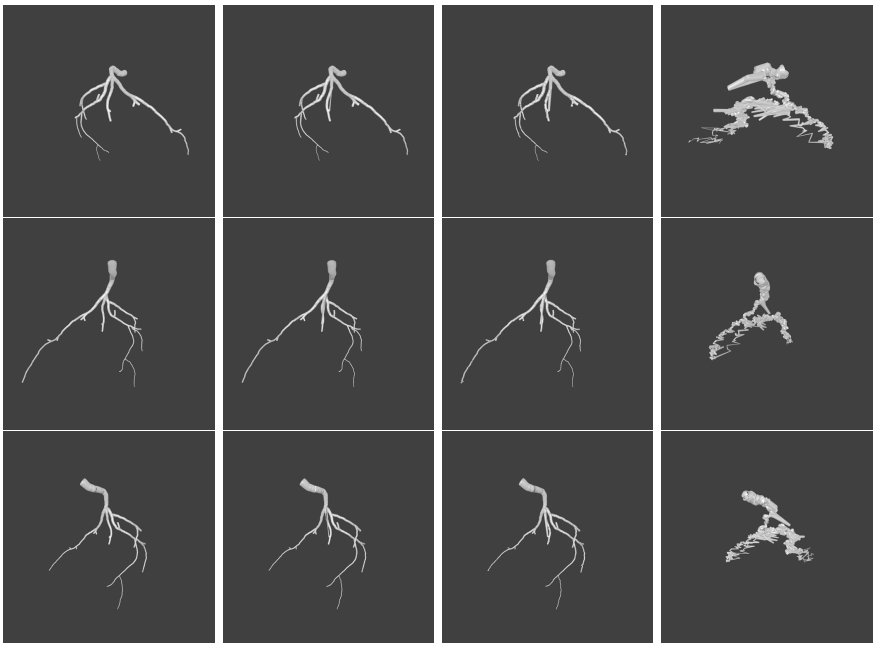

(A) Ground-Truth (B) MvFCNN (C) TDAEn_Dense (D) En_LSTM_Dec

FIGURE 7. The prediction of proposed networks for qualitative comparisons (test data o00015). Rows show the same object from different views.

4.2. **Qualitative Comparison for 3D Reconstruction.** We depict the reconstruction performances of each network in Fig. 7. It is clear from the figure that LSTM-based network produces worse predictions than CNN based networks. We

observe that they fail to learn to estimate 3D positions of centers and corresponding radius of coronaries. The reasons why LSTM-based networks failed are discussed previously in Section 4.1.

If we compare predictions qualitatively, we observe that MvFCNN and TDAEn_Dense networks perform well on 3D reconstruction. There is no difference visually worth mentioning but quantitative comparison in Table 1 shows that MvFCNN produces, on average, 3.3 times better than TDAEn_Dense in CD metric and 25.27 times better in radius estimates. En_LSTM_Dec has the worst 3D reconstruction performance. It fails to construct the structure of coronary artery anatomy (see Fig. 7). We consider this is because LSTMs are not appropriate choice for auto-regression type problem.

4.3. **Execution Time.** The experiments for running time have been implemented on two Linux-based machines. The first one is a notebook computer with the hardware specifications: Intel(R) Core (TM) i7-4700HQ CPU@2.40GHz and 16GB 1600 MHz DDR3 RAM. We use this machine for testing CPU-based platforms. The second one is a server machine where training is achieved. The hardware specifications of this machine are as follows: Xeon(R) CPU E5-2667v4 (3.20GHz) CPU, 128GB of RAM and NVIDIA Tesla P100 Graphics Processing Unit (GPU). We use this machine for testing GPU-based platforms.

In order to compare network complexities, the total number of trainable parameters and the number of CNN layers used in each network are shared in Table 2. TDAEn_Dense appears to have the most parameters but this is because it uses copies of network to calculate prediction and combines all results in dense layer (see Fig. 5). Therefore, the number of parameters in dense layer increases. The latent size for LSTM based network is 1500, however, the internal structure of LSTM is more complex than just a single metric. It has 5 different gate calculations for updating its memory and output. The running time complexities validates this computational complexity as demonstrated in Table 3.

TABLE 2. Total number of parameters for each network.

Metric / Model Name	**MvFCNN**	**TDAEn_Dense**	**En_LSTM_Dec**
Num. of Convolutional Layers	14	20	28
Num. of Dense Layer	1	1	0
Num. of Trainable Parameters	304,201,808	626,246,480	311,528,065

We measure prediction time on test data for each network and calculate its average over 3000 samples. Table 3 reports the average running-time on CPU and GPU based platforms for a single prediction.

Since memory-based (LSTM) network are larger (more complex, more weights, more calculation), it produces prediction slower than the other two networks. If we compare run-time for different platforms, GPU based platform produces at least

TABLE 3. Run-time comparison of proposed networks on CPU and GPU based platforms.

Model Name	**CPU (seconds)**	**GPU (seconds)**	**Ratio (CPU / GPU)**
MvFCNN	0.033588	0.001923	17.47
TDAEn_Dense	0.120523	0.004286	28.12
En_LSTM_Dec	0.243891	0.005843	41.74

17.47 times faster than CPU based platform on average. This gain increases to 41.74 for larger and more complex deep networks. The fastest network appears to be MvFCNN with approximately 30 and 520 predictions per second on CPU and GPU, respectively.

5. Conclusion

In this paper, we have proposed deep-learning based 3D reconstruction method from 2D X-Ray angiograms for coronary arterial tree. Previously, this problem is solved using analytical methods in the related literature but such methods have some limitations discussed earlier in Section 1. We have solved the same problem with a learning-based approach. In this study, for the first time in literature, we demonstrate that coronary arteries can be reconstructed using 3D deep networks. We have proposed variations of 3D-R2N2 network [27] and multi-view CNN based networks. 3D-R2N2 network produces voxel-grids and the resolution is very low. It is not appropriate for our problem. Thus, we modify object representation and present well-defined data-structure for 3D representation of objects in tubular/cylindrical shapes described in Section A. We have shown that networks can learn this representation and show promising results. We prove the validation of the data-structure and architectures proposed in this study for 3D reconstruction of coronaries.

In this study, 3D reconstruction task is designed as a regression problem in which output contains continuous values. We conduct experimental tests to quantitatively evaluate and compare the performance of networks. We observe that CNN-based networks yield better 3D reconstruction performances in terms of CD and MSE metrics. The results for memory-based network (LSTM) are worse than CNN only-based networks and memory-based network fails to construct coronary tree anatomy. We consider this is because memory-based networks must remember past observations thanks to their internal cells whereas CNN-based networks are provided this data explicitly. We conclude that LSTMs are not appropriate for auto-regression problems as stated in [6].

We show and validate our 3D reconstruction method in this study using a synthetic data-set produced from real subjects. We believe that 3D reconstruction with deep learning architecture can be improved further with the evaluation of

technologies and development of variants of network architectures. We believe that the topic (DL-based 3D reconstruction) becomes a trending problem shortly which is already started with object reconstruction.

5.1. **Limitations and Future Work.** We consider 3D reconstruction problem as a regression problem in this study. We train networks to estimate 6000 floating point numbers from their inputs. This is a difficult task. Instead, a deformable model can be used to facilitate the 3D reconstruction problem, as the anatomy of the heart vessels is specific. This kind of approach will decrease the number of parameters in networks and we believe that the performance will improve on 3D reconstruction.

Secondly, one may use transfer learning method to train (fine-tuning) our network on real coronary data. Since there is no publicly available X-Ray coronary data-set, we hope this study encourages researchers to share their X-Ray angiogram data with the community.

Vessel construction method presented in this study can also be applicable to other forms of vessels such as retinal images. Researchers are encouraged to try tubular shape representation in their work.

Author Contribution Statements The authors jointly worked on the study. All authors read and approved the final copy of the manuscript.

Declaration of Competing Interests The authors declare that there is no conflict of interest regarding the publication of this article.

Acknowledgement We would like to thank Professor Pablo Javier Blanco for sharing his research data (3D coronary centerlines) with us. This data enabled us to progress rapidly in deep-learning-based 3D reconstruction in our work.

This study is based on Ph.D. thesis of İ. Atli and is supported by Ankara Yildirim Beyazit University BAP, Turkey under the project number 3809.

References

[1] World health organization, `https://www.who.int/news-room/fact-sheets/detail/cardiovascular-diseases-(cvds)`, Accessed: 2020-07-22.

[2] Xiao, R., Yang, J., Fan, J., Ai, D., Wang, G., Wang, Y., Shape context and projection geometry constrained vasculature matching for 3d reconstruction of coronary artery, *Neurocomputing, 195* (2016), 65–73, https://dx.doi.org/10.1016/j.neucom.2015.08.110.

[3] Zheng, S., Meiying, T., Jian, S., Sequential reconstruction of vessel skeletons from x-ray coronary angiographic sequences, *Comput. Med. Imaging Graph., 34* (5) (2010), 333–345, https://dx.doi.org/10.1016/j.compmedimag.2009.12.004.

[4] Fazlali, H. R., Karimi, N., Soroushmehr, S. M. R., Sinha, S., Samavi, S., Nallamothu, B., Najarian, K., Vessel region detection in coronary x-ray angiograms, In *Proc. - Int. Conf. Image Process. ICIP (ICIP)* (2015), IEEE, pp. 1493–1497, https://dx.doi.org/0.1109/ICIP.2015.7351049.

[5] Medical radiation, `https://www.medicalradiation.com/types-of-medical-imaging/imaging-using-x-rays/angiography/`, Accessed: 2020-07-23.

[6] Gers, F. A., Eck, D., Schmidhuber, J., Applying lstm to time series predictable through time-window approaches, In *Neural Nets WIRN Vietri-01*, Springer, 2002, pp. 193–200, https://dx.doi.org/10.1007/978-1-4471-0219-9_20.

[7] Cong, W., Yang, J., Ai, D., Chen, Y., Liu, Y., Wang, Y., Quantitative analysis of deformable model-based 3-d reconstruction of coronary artery from multiple angiograms, *IEEE Trans. Biomed. Eng., 62* (8) (2015), 2079–2090, https://dx.doi.org/10.1109/TBME.2015.2408633.

[8] Yang, J., Cong, W., Chen, Y., Fan, J., Liu, Y., Wang, Y., External force back-projective composition and globally deformable optimization for 3-d coronary artery reconstruction, *Phys. Med. Biol., 59* (4) (2014), 975, https://dx.doi.org/10.1088/0031-9155/59/4/975.

[9] Chen, S. J., Carroll, J. D., 3-d reconstruction of coronary arterial tree to optimize angiographic visualization, *IEEE Trans. Med. Imag., 19* (4) (2000), 318–336, https://dx.doi.org/10.1109/42.848183.

[10] Chen, S.-Y., Carroll, J. D., Kinematic and deformation analysis of 4-d coronary arterial trees reconstructed from cine angiograms, *IEEE Trans. Med. Imag., 22* (6) (2003), 710–721, https://dx.doi.org/10.1109/TMI.2003.814788.

[11] Andriotis, A., Zifan, A., Gavaises, M., Liatsis, P., Pantos, I., Theodorakakos, A., Efstathopoulos, E. P., Katritsis, D., A new method of three-dimensional coronary artery reconstruction from x-ray angiography: Validation against a virtual phantom and multislice computed tomography, *Catheter. Cardiovasc. Interv., 71* (1) (2008), 28–43, https://dx.doi.org/10.1002/ccd.21414.

[12] Yang, J., Wang, Y., Liu, Y., Tang, S., Chen, W., Novel approach for 3-d reconstruction of coronary arteries from two uncalibrated angiographic images, *IEEE Trans. Image Process., 18* (7) (2009), 1563–1572, https://dx.doi.org/10.1109/TIP.2009.2017363.

[13] Liu, X., Hou, F., Hao, A., Qin, H., A parallelized 4d reconstruction algorithm for vascular structures and motions based on energy optimization, *Vis. Comput., 31* (11) (2015), 1431–1446, https://dx.doi.org/10.1007/s00371-014-1024-4.

[14] Sarry, L., Boire, J.-Y., Three-dimensional tracking of coronary arteries from biplane angiographic sequences using parametrically deformable models, *IEEE Trans. Med. Imag., 20* (12) (2001), 1341–1351, https://dx.doi.org/10.1109/42.974929.

[15] Cañero, C., Vilariño, F., Mauri, J., Radeva, P., Predictive (un) distortion model and 3-d reconstruction by biplane snakes, *IEEE Trans. Med. Imag., 21* (9) (2002), 1188–1201, https://dx.doi.org/10.1109/TMI.2002.804421.

[16] Hoffmann, K. R., Sen, A., Lan, L., Chua, K.-G., Esthappan, J., Mazzucco, M., A system for determination of 3d vessel tree centerlines from biplane images, *Int. J. Card. Imag., 16* (5) (2000), 315–330, https://dx.doi.org/10.1023/A:1026528209003.

[17] Shechter, G., Devernay, F., Coste-Manière, E., Quyyumi, A., McVeigh, E. R., Three-dimensional motion tracking of coronary arteries in biplane cineangiograms, *IEEE Trans. Med. Imag., 22* (4) (2003), 493–503, https://dx.doi.org/10.1109/TMI.2003.809090.

[18] Fallavollita, P., Cheriet, F., Optimal 3d reconstruction of coronary arteries for 3d clinical assessment, *Comput. Med. Imaging Graph., 32* (6) (2008), 476–487, https://dx.doi.org/10.1016/j.compmedimag.2008.05.001.

[19] Wiesent, K., Barth, K., Navab, N., Durlak, P., Brunner, T., Schuetz, O., Seissler, W., Enhanced 3-d-reconstruction algorithm for c-arm systems suitable for interventional procedures, *IEEE Trans. Med. Imag., 19* (5) (2000), 391–403, https://dx.doi.org/10.1109/42.870250.

[20] Liao, R., Luc, D., Sun, Y., Kirchberg, K., 3-d reconstruction of the coronary artery tree from multiple views of a rotational x-ray angiography, *Int. J. Card. Imag., 26* (7) (2010), 733–749, https://dx.doi.org/10.1007/s10554-009-9528-0.

[21] Torr, P. H., Murray, D. W., The development and comparison of robust methods for estimating the fundamental matrix, *Int. J. Comput. Vis., 24* (3) (1997), 271–300, https://dx.doi.org/10.1023/A:1007927408552.

[22] Navaneet, K., Mandikal, P., Agarwal, M., Babu, R. V., Capnet: Continuous approximation projection for 3d point cloud reconstruction using 2d supervision, In *Proceedings of the AAAI Conference on Artificial Intelligence* (2019), vol. 33, pp. 8819–8826, https://dx.doi.org/10.1609/aaai.v33i01.33018819.

[23] Fan, H., Su, H., Guibas, L. J., A point set generation network for 3d object reconstruction from a single image, In *CVPR* (2017), pp. 605–613.

[24] Zamorski, M., Zieba, M., Klukowski, P., Nowak, R., Kurach, K., Stokowiec, W., Trzciński, T., Adversarial autoencoders for compact representations of 3d point clouds, *Comput. Vis. Image Underst., 193* (2020), 102921, https://dx.doi.org/10.1016/j.cviu.2020.102921.

[25] Lun, Z., Gadelha, M., Kalogerakis, E., Maji, S., Wang, R., 3d shape reconstruction from sketches via multi-view convolutional networks, In *Proc. - 2017 Int. Conf. 3D Vis. (3DV)* (2017), IEEE, pp. 67–77, https://dx.doi.org/10.1109/3DV.2017.00018.

[26] Arsalan Soltani, A., Huang, H., Wu, J., Kulkarni, T. D., Tenenbaum, J. B., Synthesizing 3d shapes via modeling multi-view depth maps and silhouettes with deep generative networks, In *CVPR* (2017), pp. 1511–1519.

[27] Choy, C. B., Xu, D., Gwak, J., Chen, K., Savarese, S., 3d-r2n2: A unified approach for single and multi-view 3d object reconstruction, In *ECCV* (2016), Springer, pp. 628–644, https://dx.doi.org/10.1007/978-3-319-46484-8_38.

[28] Riegler, G., Osman Ulusoy, A., Geiger, A., Octnet: Learning deep 3d representations at high resolutions, In *CVPR* (2017), pp. 3577–3586.

[29] Tatarchenko, M., Dosovitskiy, A., Brox, T., Octree generating networks: Efficient convolutional architectures for high-resolution 3d outputs, In *Proc. IEEE Int. Conf. Comput. Vis.* (2017), pp. 2088–2096.

[30] Yan, X., Yang, J., Yumer, E., Guo, Y., Lee, H., Perspective transformer nets: Learning single-view 3d object reconstruction without 3d supervision, In *Adv. Neural Inf. Process. Syst.* (2016), pp. 1696–1704.

[31] Wang, P.-S., Liu, Y., Guo, Y.-X., Sun, C.-Y., Tong, X., O-cnn: Octree-based convolutional neural networks for 3d shape analysis, *ACM Trans. Graph., 36* (4) (2017), 1–11, https://dx.doi.org/10.1145/3072959.3073608.

[32] Xie, H., Yao, H., Sun, X., Zhou, S., Tong, X., Weighted voxel: a novel voxel representation for 3d reconstruction, In *Proceedings of the 10th International Conference on Internet Multimedia Computing and Service* (2018), pp. 1–4, https://dx.doi.org/10.1145/3240876.3240888.

[33] Häne, C., Tulsiani, S., Malik, J., Hierarchical surface prediction for 3d object reconstruction, In *Proc. - 2017 Int. Conf. 3D Vis. (3DV)* (2017), IEEE, pp. 412–420, https://dx.doi.org/10.1109/3DV.2017.00054.

[34] Paschalidou, D., Ulusoy, O., Schmitt, C., Van Gool, L., Geiger, A., Raynet: Learning volumetric 3d reconstruction with ray potentials, In *CVPR* (2018), pp. 3897–3906.

[35] Wang, N., Zhang, Y., Li, Z., Fu, Y., Liu, W., Jiang, Y.-G., Pixel2mesh: Generating 3d mesh models from single rgb images, In *ECCV* (2018), pp. 52–67.

[36] Pontes, J. K., Kong, C., Sridharan, S., Lucey, S., Eriksson, A., Fookes, C., Image2mesh: A learning framework for single image 3d reconstruction, In *Asian Conference on Computer Vision* (2018), Springer, pp. 365–381, https://dx.doi.org/10.1007/978-3-030-20887-5_23.

[37] Tatarchenko, M., Dosovitskiy, A., Brox, T., Multi-view 3d models from single images with a convolutional network, In *ECCV* (2016), Springer, pp. 322–337, https://dx.doi.org/10.1007/978-3-319-46478-7_20.

[38] Girdhar, R., Fouhey, D. F., Rodriguez, M., Gupta, A., Learning a predictable and generative vector representation for objects, In *ECCV* (2016), Springer, pp. 484–499, https://dx.doi.org/10.1007/978-3-319-46466-4_29.

[39] Chang, A. X., Funkhouser, T., Guibas, L., Hanrahan, P., Huang, Q., Li, Z., Savarese, S., Savva, M., Song, S., Su, H., et al., Shapenet: An information-rich 3d model repository, *arXiv preprint arXiv:1512.03012* (2015).

[40] Everingham, M., Van Gool, L., Williams, C., Winn, J., Zisserman, A., The pascal visual object classes challenge 2012 (voc2012), *Results* (2012).

[41] Blanco, P. J., Bulant, C. A., Müller, L. O., Talou, G. M., Bezerra, C. G., Lemos, P., Feijóo, R. A., Comparison of 1d and 3d models for the estimation of fractional flow reserve, *Sci. Rep., 8* (1) (2018), 1–12, https://dx.doi.org/10.1038/s41598-018-35344-0.

[42] Horn, F., Leghissa, M., Kaeppler, S., Pelzer, G., Rieger, J., Seifert, M., Wandner, J., Weber, T., Michel, T., Riess, C., et al., Implementation of a talbot-lau interferometer in a clinical-like c-arm setup: A feasibility study, *Sci. Rep., 8* (1) (2018), 1–11, https://dx.doi.org/10.1038/s41598-018-19482-z.

Appendix

Appendix A. Transformation of Tubular Shapes to 3D

There are various ways to represent objects in 3D and 3D representation matters in terms of 3D machine learning. A compatible data structure with deep learning method can improve reconstruction performance of networks. Thus, we define a new data structure for holding tubular shapes specifically. In this structure, the center of circles and their radii are used to represent tubular shapes. The center points must come sequentially to obtain the path for a continuous tubular shape (see Fig. 8). In this way, we can find the direction of each consecutive circle using[1]:

$$\vec{n} = \frac{\overrightarrow{C_i C_{i+1}}}{\left\|\overrightarrow{C_i C_{i+1}}\right\|} = \frac{C_{i+1} - C_i}{\|C_{i+1} - C_i\|} \tag{2}$$

The segment shown in Fig. 8 starts with its center point (C_0) in 3D space and ends with the corresponding radius (r_0) of the circle centered at C_0 for the first line. We assume that this segment is continuous until the end of the segment sign (?, ?, ?, -1) appears. We represent the end of the segment with ?, ?, ? for indicating any value for center point and a negative value for radius (it is -1 in the example). The direction of tubular segments can easily be derived (using Eq. 2) from the continuity assumption in which center points must come in order (see Fig. 8).

In order to recover tubular shape, we need to sample points around centers with a given radius as in Fig. 8. $\vec{u}$ and $\vec{v}$ vectors are on the surface of the circle and can be derived with a little effort using equations 3, 4, 5 and 6. The variables n_x and n_y in the equations show unit normal values in X and Y directions, respectively. For deeper understanding of vectors in 3D space along with 3D reconstruction, please have a look at this book[2].

$$\vec{n} = \langle x, y, z \rangle \tag{3}$$

[1]Olver, Peter J., Chehrzad Shakiban, and Chehrzad Shakiban. Applied linear algebra. Prentice Hall, 2006

[2]Andrew, Alex M. "Multiple view geometry in computer vision." Kybernetes (2001)

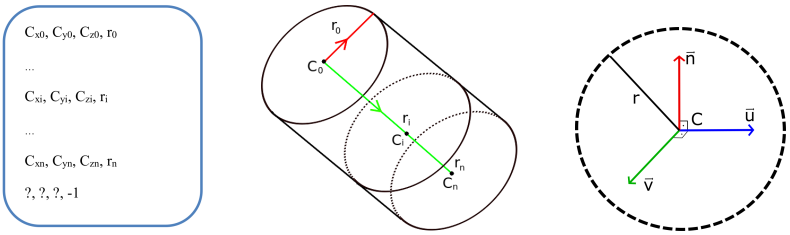

FIGURE 8. Tubular shape representation for one segment. C_i and r_i show center and radius for the point at location i. For sampling tubular shapes around centers (on the right), $\vec{n}$ shows unit normal to the surface, $\vec{u}$ and $\vec{v}$ are perpendicular unit vectors lie on the surface of the circle.

$$\vec{t} = \langle n_x, -n_y, 0 \rangle \tag{4}$$

$$\vec{u} = \vec{n} \times \vec{t} \tag{5}$$

$$\vec{v} = \vec{n} \times \vec{u} \tag{6}$$

We parametrize the circle using these vectors ($\vec{u}$ and $\vec{v}$) around each center point C_i to obtain represented 3D cylindrical shape. In our tests, we sampled each circle with 20 points. If desired, this can be increased for a better resolution of tubular shapes. Parametrization over the angle, θ, can be achieved as follows:

$$P_{s_i} = (r * cos\theta)\vec{u} + (r * sin\theta)\vec{v} + C_i \tag{7}$$

where P_{s_i} is an array of sampled points for $0 \leq \theta \leq 2\pi$ with a step of $2\pi/20$ and C_i is i^{th} center point in the segment.

APPENDIX B. MULTI-VIEW IMAGE GENERATION

Remembering the main goal posed at the beginning of this study, we propose deep-learning based 3D reconstruction method for coronary arteries from 2D X-Ray angiograms to provide an objective, reproducible clinical assistance. To achieve this goal, we have generated 3D coronaries synthetically with the procedure mentioned in Section 3.1. The next step is to produce multi-view images of coronaries. We have created a tool for producing multiple images from different views of angle like in X-Ray C-arm machine. We simulate 2 axis rotations demonstrated in Fig. 9. The coordinates of the camera (head point of C-arm) after rotations are calculated using spherical coordinates as follows:

$$\langle C_x, C_y, C_z \rangle = \langle \rho \sin(\theta), \rho \cos(\theta), \rho \sin(\theta) \cos(\psi) \rangle \tag{8}$$

where ρ is the distance between the camera and the geometric center of objects (coronaries). We use Blender software[3] to produce multiple-view images (n=3) of coronary arterial tree. Since operators capture X-Ray images in variety of angles to visualize blood vessels clearly, we use random rotations during the generation of multi-view images.

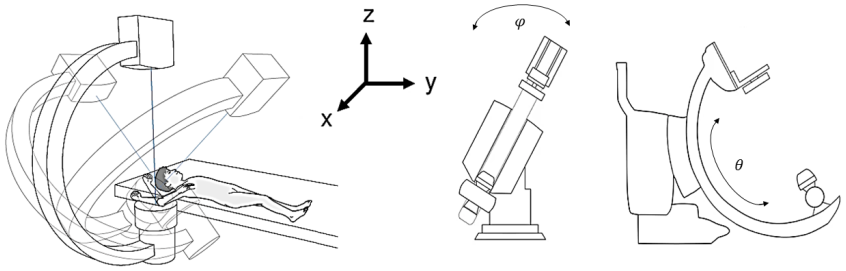

FIGURE 9. C-arm rotation axis simulation. θ and ψ represent rotations in y-axis and x-axis, respectively [42].

[3]www.blender.org

http://communications.science.ankara.edu.tr

Commun.Fac.Sci.Univ.Ank.Series A2-A3
Volume 64, Number 1, Pages 21-39 (2022)
DOI: 10.33769/aupse.1068297
ISSN 1303-6009 E-ISSN 2618-6462

Research Article; Received: Feburary 04, 2022; Accepted: Feburary 24, 2022

THE EFFECTS OF DC OFFSET IN DIRECT-CONVERSION RECEIVERS FOR WLAN SYSTEMS

Yunus Emre ŞEN[1] and Selçuk TAŞCIOĞLU[2]

[1]Department of Electrical and Electronics Engineering,
Gazi University, Ankara, TURKEY
[2]Department of Electrical and Electronics Engineering,
Ankara University, Ankara, TURKEY

ABSTRACT. In this paper, the effects DC offset in direct-conversion receivers for WLAN systems are analyzed using both experimental and simulation data. DC offset estimation is performed by using data-aided methods which are based on the short training sequence of WLAN preamble. In the simulations, DC offset and frequency offset estimations are carried out on the signals affected by frequency selective Rayleigh fading channel and additive white Gaussian noise. Estimation performance of the methods is compared for different SNR levels and frequency offset values in terms of mean square error. Experimental data which is in the form of WLAN packets and transmitted through a wireless channel is captured by using a software defined radio. The experimental performance of the DC offset compensation methods is evaluated in terms of transmission success ratio.

1. INTRODUCTION

With the increasing demand for mobile communication and the reduction in the size of wireless communication devices over time have led to some developments in receiver architectures. As a result of these developments, new generation receivers with simpler architecture and lower power consumption have emerged. The most popular receiver architecture with these features is the direct-conversion receiver architecture [1]. Unlike traditional heterodyne receivers, nonintegrable RF filters are not required in direct-conversion receivers, which reduces the cost and dimension of the system. However, these receivers have some disadvantages caused by their architecture which reduces the system performance. The advantages and disadvantages of traditional and new generation wireless receiver architectures have

Keywords. DC offset, direct-conversion receivers, frequency offset, WLAN, software defined radio.
yunusemresen@gazi.edu.tr; selcuk.tascioglu@eng.ankara.edu.tr-Corresponding author
0000-0001-5103-3388; 0000-0001-9064-2960.

been discussed considering compatibility with the integrated circuits in [1,2]. Designing issues of the direct-conversion receivers were described and circuit techniques for alleviating the disadvantages of this architecture were proposed in [3].

One of the most serious problems of direct-conversion receivers is the DC offset which causes distortion when the RF spectrum is downconverted to the baseband [4]. Large values of the DC offset would saturate the receiver front-end, which may cause the signal not to be properly amplified. Therefore, the DC offset significantly affects the dynamic range of the receiver and accordingly its sensitivity. Even a small amount of DC offset, if not compensated, may degrade the performance of a direct-conversion receiver by causing estimation errors for the parameters in detection and decoding stages [5]. Besides, the performance loss due to DC offset is expected to be more serious for high order modulation techniques [5]. Therefore, DC offset should be properly compensated in direct-conversion receivers working in wireless networks to provide a reliable communication, especially at high data rates where high order modulation is required.

DC offset arises in direct-conversion receivers due to different reasons. Basically, the leakage signals that occur as a result of the imperfect isolation between the components in the receiver circuit generate DC offset [2,3]. Due to imperfect isolation in the receiver, the local oscillator (LO) signal leaks from the mixer and appears at the input of the mixer on the low noise amplifier (LNA) side as shown in Fig. 1. The leakage signal is multiplied by itself, which is called self-mixing. Depending on impedances between the components in the receiver, the leakage signals may be observed at the input of the mixer, as well as they may be transmitted from the antenna and reflected from the objects in the environment and returned to the receiver again. DC offset is also observed when a large interference signal leaks into the local oscillator port and is multiplied by itself at the mixer [3]. Leakage signals causing DC offset are shown in Fig. 1. In this figure, dashed curves denote leakage signals and dotted curve indicates interference signal.

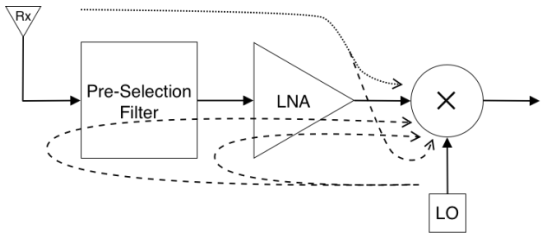

FIGURE 1. Origin of DC offset [2].

In order to increase the performance of the direct-conversion receivers, DC offset may be compensated by using analog or digital signal processing methods. In analog methods, an ideal DC offset cancellation circuit is desired to act as a high-pass filter with an infinite attenuation at the DC, while passing the desired signal spectrum without distortion [6]. These methods simultaneously update the estimates as the DC offset changes in time, which makes them attractive for real time applications. The simplest analog method is AC-coupling which uses a DC block capacitor and a resistor to form a high-pass filter character. This method can be used for modulation schemes where the spectrum of the signal is located away from DC. However, circuit design with the requirement of low attenuation on the desired band increase the power consumption and chip area, which is not suitable for new generation low-cost receivers [6].

In order to simplify the circuit design and increase the integration level of the receivers, several digital signal processing techniques have been employed [5, 7-11]. In these methods, DC offset estimation task has been performed after digitizing the signal by an analog-to-digital converter.

In [7], a digital signal processing technique based on least-squares estimation was proposed to mitigate the effects of DC offset and IQ mismatch in direct-conversion receivers. It was shown by simulations that the method has a good performance for frequency-selective channels. In [8], IQ imbalance, DC offset, and channel response were estimated jointly for an orthogonal frequency division multiplexing (OFDM) system. The estimations were performed by one OFDM block which is arbitrarily chosen for training. The authors demonstrated through simulations that the performance of the proposed method was similar to the performance in case of perfect information about these parameters. In [9-11], data-aided DC offset estimation methods which can be employed in OFDM based WLAN systems were proposed.

In this paper, three existing DC offset estimation methods for OFDM-based WLAN systems have been implemented and compared through simulations in terms of mean square error (MSE). We also implemented the mean subtraction approach on WLAN signals for a baseline comparison. The effect of DC offset cancellation methods on the wireless communication performance in a real system has also been measured. The experimental performance evaluation of the methods has been obtained by applying the methods to the signals transmitted by a software defined radio.

The outline of the paper is as follows: In Section 2, problem definition for DC offset problem is introduced. In Section 3, carrier frequency offset estimation methods used in this paper are presented. In Section 4, motivation for why CFO and DC offset problems should be addressed together is explained and DC offset estimation methods used in this paper are given. Simulation and experimental results are presented in Section 5 and Section 6, respectively. Section 7 concludes the paper.

2. Problem Definition

The discrete baseband signal model for one OFDM symbol length excluding the cyclic prefix is given by

$$y(n) = h(n) * x(n) + w(n) + d, \quad n = 1,2,\ldots,N \tag{1}$$

where n is discrete time index, N is the number of subcarriers in the OFDM system, $x(n)$ denotes transmitted signal, $h(n)$ and $w(n)$ are additive white Gaussian noise and channel response, respectively, and d is the DC offset. For the direct conversion receiver architecture, quadrature mixing is used in which real DC offset occurs in quadrature branches. Quadrature signals are represented as $I + jQ$ to form the complex baseband signal for digital signal processing, in which case DC offset is also represented as a complex number. Mathematical expression for the DC offset resulting from the self-mixing can be given as

$$A_1\cos(\omega_{LO}t)\,A_2\cos(\omega_{LO}t) = \underbrace{\frac{A_1A_2}{2}}_{DC\ Term} + \frac{A_1A_2}{2}\cos(2\omega_{LO}t) \tag{2}$$

where sinusoidal terms at the left hand side of the equation are LO signal and leakage version of this signal at the input of the mixer. A_1 and A_2 are the amplitudes and ω_{LO} is the frequency of these signals. This multiplication results in a high frequency and a DC term. The high frequency term can be removed by filtering out since the desired signal is downconverted to the baseband, however the DC component causes a distortion when the desired signal contains energy at DC.

In this paper, DC offset problem and the compensation methods are considered for the OFDM based WLAN signals having non-high throughput (non-HT) transmission vector format preambles [12]. The data-aided compensation methods considered herein use a part of the legacy short training field (L-STF) of the WLAN preamble. This signal part is extracted from the first OFDM symbol by removing the cyclic prefix. For channel bandwidth of 20 MHz and $N = 64$ subcarriers, L-STF is constructed from two identical OFDM symbols of length 160 samples. After removing the 16-length cyclic prefix from the first OFDM symbol, the signal part used for DC offset estimation is obtained as

$$r = \left[y(17) \ \ldots \ y(80) \right]^T \tag{3}$$

Time domain average of the received signal is defined as follows

$$\widehat{d} = \sum_{n} y(n) \tag{4}$$

(4) can be used as a DC offset estimation and DC component can be simply eliminated using mean subtraction (MS) approach. This approach is used in the literature in various forms. For example, in [13] DC offset is estimated by using a blind method having two stages. At the first stage of this method, mean subtraction is carried out and it has been emphasized that it provides a coarse compensation. The formulation for the compensated signal $\boldsymbol{r}_0$ is given as

$$\boldsymbol{r}_0 = \left\{ \boldsymbol{I}_{N\times N} - (1/N)\, \boldsymbol{a}\boldsymbol{a}^H \right\} \boldsymbol{r} \tag{5}$$

where N=64 is the length of signal $\boldsymbol{r}$, $\boldsymbol{\alpha}$ is 64-length column vector whose all elements are equal to 1, $\boldsymbol{I}$ is 64×64 identity matrix, and $(.)^H$ denotes the Hermitian transpose of a matrix.

In this paper, mean subtraction approach is applied to 64-length L-STF signal as in other implemented methods. In this case, DC offset estimation by mean subtraction is calculated as

$$\widehat{d} = \sum_{n=0}^{N-1} r(n) \tag{6}$$

where $r(n)$ is 64-length L-STF signal part which is defined in (3).

Even though mean subtraction is easy to implement, DC offset estimation performance of this method is not good enough. Therefore, it would not be the best choice for WLAN systems. The aim of implementing the mean subtraction method is to compare the performances of the DC offset compensation methods with the performance of this baseline approach. Also, this method cannot be implemented when using a modulation scheme having DC. DC subcarrier is not used in OFDM based WLAN protocols discussed in this paper. However, for these systems there is another issue called carrier frequency offset (CFO), which must be compensated to avoid reducing system performance. Without cancelling the DC offset with a high accuracy, CFO compensation causes spreading the DC energy over the other subcarriers [5]. Therefore, CFO and DC offset problems should be addressed together. The CFO compensation can be performed after cancelling the DC offset from the received signal as follows

$$\widehat{y}(n) = (y(n) - \widehat{d})\, e^{-j2\pi n\widehat{\varepsilon}/N}, \quad n = 1, 2, \ldots, N \tag{7}$$

In the following sections CFO and DC offset estimation methods used in this paper are presented.

3. Carrier Frequency Offset Estimation

OFDM provides high data rates by using overlapping subcarriers, which makes it a common technique for WLAN systems. However, the use of overlapping subcarriers increases vulnerability to the CFO caused by the Doppler shift and the frequency mismatch between the local oscillator signals at the receiver and transmitter. The existence of CFO leads to intercarrier interference (ICI) whose effect is shown in Fig. 2 for L-STF spectrum. This figure shows that the amount of distortion changes with CFO value.

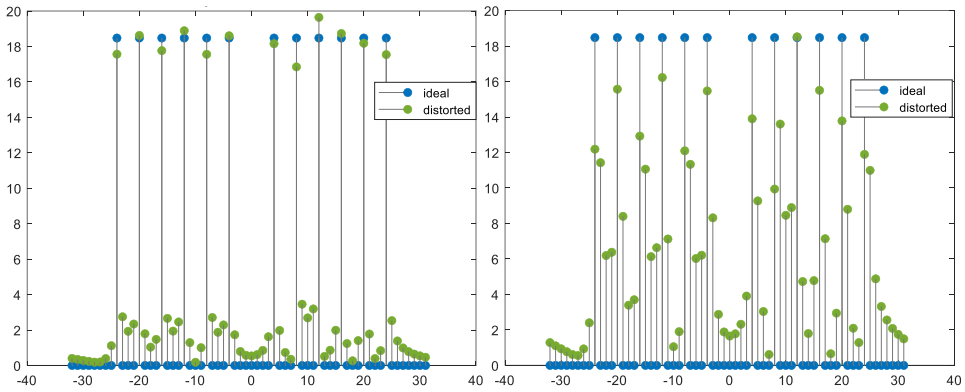

Figure 2. Distortions caused by CFO on L-STF spectrum for CFO vales of 0.1 (left) and 0.4 (right).

In this paper, simulations and experiments were performed for WLAN system with 20 MHz channel bandwidth. In this case, spacing between OFDM subcarriers is found to be as 20 MHz / 64 = 312500 Hz. Using this value, the normalized CFO is calculated as

$$\varepsilon = \frac{\Delta f}{312500} \tag{8}$$

where Δf is the CFO value in Hz.

Two different CFO estimation methods have been implemented in this paper. The first method proposed in [9] employs the same part of L-STF signal which is used for DC offset estimation and defined in (3). Two signal parts are taken from $\boldsymbol{r}$

defined as $\boldsymbol{r}_1 = [r(0), \ldots, r(48)]$ and $\boldsymbol{r}_2 = [r(16), \ldots, r(64)]$. A complex scalar R_p value is calculated from these signal parts as follows

$$R_p = L^{-1}\boldsymbol{r}_1^H \boldsymbol{r}_2 - L^{-2}\boldsymbol{r}_1^H \mathbf{1}_L \mathbf{1}_L^T \boldsymbol{r}_2 \tag{9}$$

where L is the length of $\boldsymbol{r}_1$ ve $\boldsymbol{r}_2$ vectors, $\mathbf{1}_L$ is an all 1 vector, and $(.)^T$ denotes the transpose of a matrix. By using the complex R_p value, CFO is estimated by

$$\hat{\varepsilon} = \frac{M}{2\pi} arg(R_p) \tag{10}$$

where M denotes the number of identical symbols in an OFDM symbol excluding the cyclic prefix and $arg(.)$ represents the argument of a complex number. CFO estimation can be performed in the matrix form as follows

$$\boldsymbol{r}_0 = \boldsymbol{\Gamma}_N(\hat{\varepsilon})\, \boldsymbol{r} \tag{11}$$

where $\boldsymbol{\Gamma}_N$ represents diagonal matrix defined as

$$\boldsymbol{\Gamma}_N(\hat{\varepsilon}) = diag\left\{1, e^{j\frac{2\pi\hat{\varepsilon}}{N}}, \ldots, e^{j\frac{2\pi\hat{\varepsilon}(N-1)}{N}}\right\} \tag{12}$$

CFO estimation was also carried out by using a second method which is given in the Matlab WLAN toolbox [14]. There are two CFO estimation stages namely coarse and fine in this approach. The L-STF and L-LTF fields of the WLAN preamble are used for coarse and fine CFO estimations, respectively. The sum of these estimations is subtracted from the entire WLAN packet to perform CFO compensation.

4. DC OFFSET ESTIMATION

The DC subcarrier is not used in OFDM based WLAN protocols in order to mitigate the distorting effect caused by DC offset [12]. DC offset would be easily cancelled by the mean subtraction approach if there were no CFO. However, in the presence of CFO, some part of the energy of other subcarriers carrying information leaks into the DC subcarrier. If the mean value of the signal is subtracted from itself, the information shifted to the DC region will be lost. That would reduce the system performance. Therefore, more effective DC offset estimation methods should be employed.

Fig. 3 shows the effects of distortions resulting from DC offset and CFO on L-STF spectrum as well as resulting spectrums after compensation for the CFO value of 0.4. For this visualization, DC offset is taken as $0.3+j0.3$ so that DC offset is stronger than the other subcarriers. In this way, it is aimed to observe the distorting effect clearly when the DC spreads over the other subcarriers due to CFO compensation. In this figure, blue points represent ideal spectrum when there are no distorting effects and green points denote the distorted spectrums. The signals distorted by CFO resulting from moving objects in the wireless environment, DC offset is superimposed on this signal at the direct-conversion receiver. Note that the distorted spectrums in Fig 3 (green points) are the sum of the DC offset and the distorted spectrums due to CFO in Fig. 2.

Fig. 3 also shows the compensated spectrums (red points). In the top left figure, the effect of compensation of CFO without DC offset cancellation is shown. As can be seen from this figure, CFO compensation spreads the DC energy over the other subcarriers. This will degrade the system performance. In the top right figure, the case where DC offset is estimated with a high estimation error and is cancelled prior to CFO compensation is considered. In this case the effect of DC energy over the other subcarriers is reduced compared to the case in the figure on the top left as expected. Since the estimated DC offset is removed from the signal prior to CFO compensation. For the bottom left figure, DC offset estimation is performed by using mean subtraction method. This method removes all the energy at DC including the useful energy which leaks from other subcarriers. Note that the DC component contains not only the DC offset but also the useful energy leaks from other subcarriers due to CFO. Removing this useful information causes distortion after DC offset and CFO compensations, especially at the subcarriers around DC. These distortions can be seen in the figure on the bottom left by comparing the compensated red points with the ideal blue points. Note that the subcarriers around DC are null for L-STF signal, but are used in data symbols. Therefore, this distortion may result in an increased bit error rate. Lastly, in the bottom right figure, the case where DC offset is estimated perfectly is considered. As shown from this figure, after compensating the DC offset and CFO perfectly, ideal spectrum is recovered without any loss. These figures show that the accuracy of DC offset estimation has a significant impact on the information carrying subcarriers and thus overall system performance for an OFDM based WLAN system.

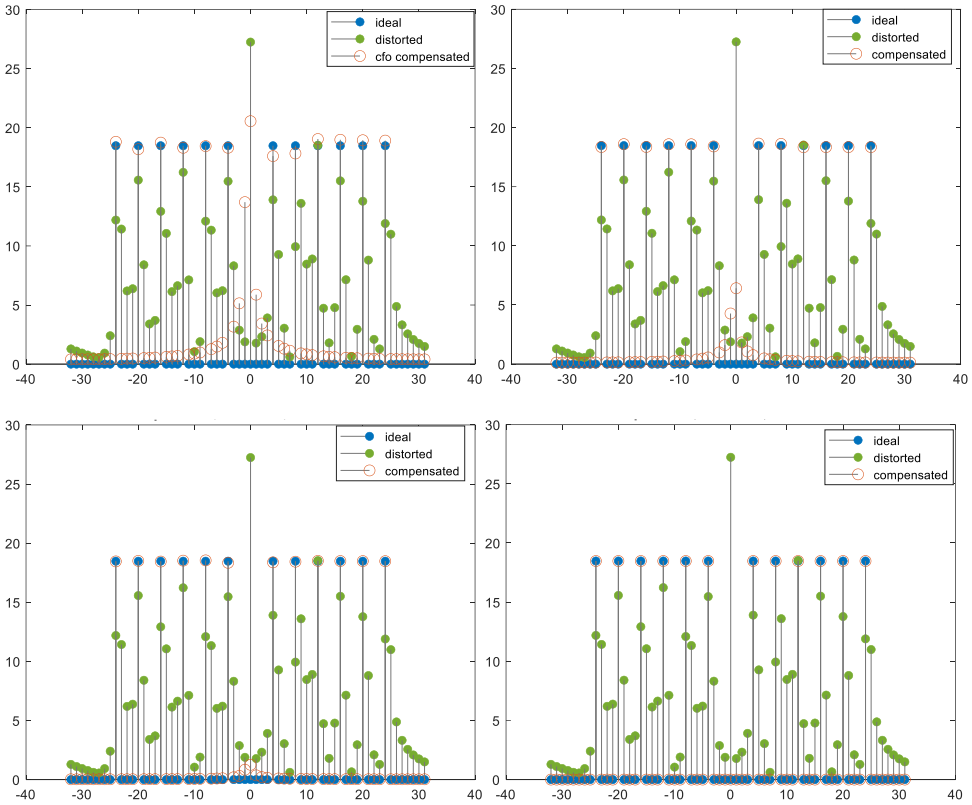

FIGURE 3. L-STF spectrums for ideal (blue), distorted (green) and compensated (red) cases. Top left: CFO compensation is performed without DC offset (DCO) cancellation. Top right: DC offset is estimated with a high estimation error and then CFO is compensated. Bottom left: DC offset estimation is performed by using mean subtraction method (MS) prior to CFO compensation. Bottom right: DC offset is estimated perfectly prior to CFO compensation.

Spectrums of two WLAN signals with (top) and without (bottom) DC offset compensation are given in Fig. 4. In the case where the DC offset is not compensated, an increase of approximately 50 dBm is observed in the power of the DC component compared to the compensated case.

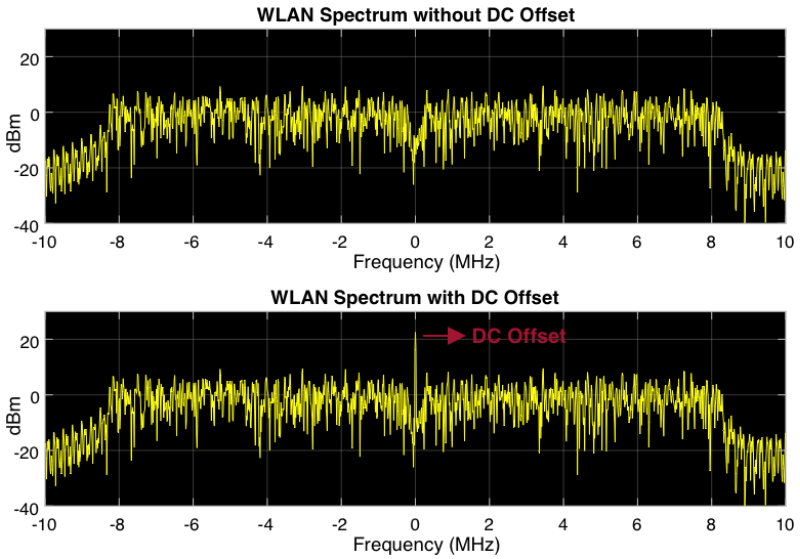

FIGURE 4. WLAN spectrum for the cases with (top) and without (bottom) DC offset compensation.

4.1. **Joint Estimation of DC Offset and CFO.** In order to achieve high performance in WLAN systems, CFO and DC offset compensations should be considered together. A method using this approach is suggested by Lin *et al*. in [9]. In this method, the estimation of the DC offset is performed by using the estimation value of CFO. Thus, high DC offset estimation performance can be achieved independent of CFO values. After estimating offset values, DC offset and CFO compensations are carried out respectively. All unloaded subcarriers are used in this method for DC offset estimation. Therefore, even at low CFO values, the energy contained in the loaded subcarriers may leak to the unloaded subcarriers used for DC offset estimation. For this reason, the CFO estimation is taken into account in the estimation of the DC offset in order to improve the estimation accuracy of the DC offset.

In this method, DC offset is estimated as

$$\hat{d} = \left[\boldsymbol{V}^H \boldsymbol{\Gamma}_N^H(\hat{\varepsilon})\, \mathbf{1}_N \right]^{\dagger} \boldsymbol{V}^H \boldsymbol{\Gamma}_N^H(\hat{\varepsilon})\, \boldsymbol{r} \tag{13}$$

where $\boldsymbol{r}$ is 64-point L-STF signal, $\boldsymbol{\Gamma}_N^H$ is the Hermitian transpose of the diagonal matrix defined in (12), $\dagger$ denotes the pseudo inverse of the matrix, $\mathbf{1}_N$ is an all 1 vector, $\hat{\varepsilon}$ is the estimated normalized CFO. $\boldsymbol{V}$ is the partition of the inverse DFT

matrix $\boldsymbol{W}$ containing only the columns corresponding to unloaded subcarriers, which can be defined as

$$\boldsymbol{V}=\left[W_{N_{1:4}}\ W_{N_{6:8}}\ \cdots\ W_{N_{26:40}}\ \cdots\ W_{N_{58:60}}\ W_{N_{62:64}}\right] \tag{14}$$

where $W_{N_{s:t}}$ represents the columns of inverse DFT matrix corresponding to unloaded subcarriers between indices s and t. Inverse DFT matrix is defined as

$$W_N=\frac{1}{\sqrt{N}}\begin{bmatrix} 1 & 1 & \cdots & 1 \\ 1 & e^{j\frac{2\pi}{N}} & \cdots & e^{j\frac{2\pi(N-1)}{N}} \\ \vdots & \vdots & \ddots & \vdots \\ 1 & e^{j\frac{2\pi(N-1)}{N}} & \cdots & e^{j\frac{2\pi(N-1)(N-1)}{N}} \end{bmatrix} \tag{15}$$

4.2. **DC Offset Estimation via Mitigating the Effect of ICI on DC Subcarrier.** The existence of CFO results in intercarrier interference (ICI) as explained in Section 3. In the L-STF field of the WLAN preamble, DC subcarriers and adjacent 3 subcarriers on the left and the right are unloaded [12]. Therefore, the amount of energy leaked on subcarriers -1, 0, 1 due to the frequency offset is relatively low and close to each other. If one can estimate the energy level leaked to DC due to ICI, then DC offset estimation can be performed with a high accuracy and independent of CFO. Xia and Ren has implemented this methodology by averaging the values of the subcarriers -1 and 1, then subtracting it from the DC component as follows [10]

$$\widehat{d}=\left[Y_0-\left(Y_1+Y_{-1}\right)/2\right]/\sqrt{N} \tag{16}$$

The values of the subcarriers -1, 0, and 1 are calculated by using the DFT formula given as

$$Y(k)=\frac{1}{\sqrt{N}}\sum_{n=0}^{N-1} r_n e^{-j2\pi nk/N},\quad k=-1,0,1 \tag{17}$$

The robustness of this method is based on the fact that the amount of the leakage energy on the DC subcarrier due to ICI can be estimated with a high accuracy by averaging the values of subcarriers -1 and 1. Note that the amount of the leakage energy on the subcarriers -1, 0, and 1 are low and close to each other since the loaded

L-STF subcarriers are sparsely located. This approach provides a DC offset estimation independent of the amount of CFO.

4.3. **DC Offset Estimation Using Linear Unbiased Estimator.** In [11], Marsili has proposed a linear unbiased estimator for DC offset estimation. This method uses the estimation coefficients defined as

$$\boldsymbol{a} = \frac{1}{\mathbf{1}^T \boldsymbol{C}^{-1} \mathbf{1}} \{\boldsymbol{C}^{-1} \mathbf{1}\} \tag{18}$$

where $\boldsymbol{C}$ is the correlation matrix, $(\,.\,)^{-1}$ denotes the inverse of a matrix, $\mathbf{1}$ is the $N \times 1$ vector whose elements are equal to 1. The correlation matrix contains the information about the WLAN preamble and CFO information which is modeled as a uniform random variable. By using the estimation coefficients defined in (18), DC offset is estimated as

$$\widehat{d} = \boldsymbol{a}^T \boldsymbol{r} \tag{19}$$

Since the CFO is modeled as a random variable in this method, the performance of the method is based on the interval defined for this random variable. That means the performance of the method increases as the prior information about CFO increases.

5. Simulation Results

In simulations, 64 QAM OFDM based WLAN signals with non-HT preambles were generated and passed through a frequency selective Rayleigh fading channel with 6 paths. The channel has an exponential power delay profile, a root mean square (RMS) delay spread of 100 ns [10] and 50 Hz maximum Doppler shift. Additive white Gaussian noise was added to the generated signals to simulate different SNR levels after adding CFO and DC offset. CFO and DC offset estimations were performed and estimation performances were evaluated using mean square error (MSE). MSE values were calculated over 10000 Monte Carlo iterations in each of which noise and channel were generated randomly.

5.1. **CFO Estimation Performance.** The performances of CFO estimation methods were compared for different SNR and CFO values in terms of MSE. As seen from Fig. 5, the performance of the Lin's method in [9] remains the same with varying CFO values. The MSE performance of the estimator in Matlab WLAN toolbox, which has two stages as explained in Section 3, increases for integer-valued CFOs and is the similar to the Lin's method for the CFO values away from integers. The

performance of both the methods significantly decreases at the normalized CFO values of -2 and 2. This can be explained as the energy of the subcarriers carrying information in the L-STF spectrum shown in Fig. 2 is shifted to the center point of these subcarriers as a result of CFO. In this case the estimation errors take the largest values.

The effect of SNR on the MSE performance of the CFO estimation methods was also evaluated for two different CFO values of 0.4 and 0.001. The performance of the Lin's method remains the same as the CFO values change in the interval [-1.9, 1.9]. The performance of the method defined in Matlab WLAN toolbox increases as the SNR increases for the normalized CFO value of 0.001. When the normalized CFO value is 0.4, the performance remains constant above 20 dB.

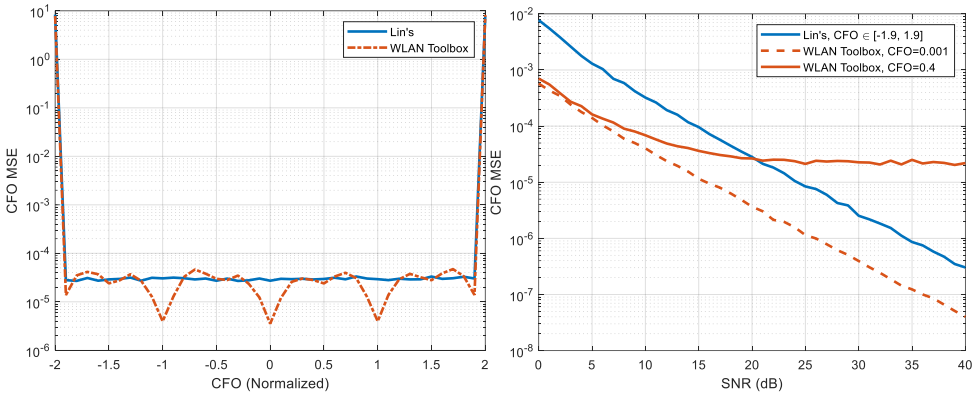

FIGURE 5. MSE of CFO estimation versus CFO (left) and SNR (right) values. DC offset is taken 0.1+*j*0.1 for both cases and SNR is taken as 20 dB for MSE versus CFO graph (left).

5.2. **DC Offset Estimation Performance.** DC offset estimation performances of the methods were evaluated for different CFO values and visualized in Fig. 6 (left). The performances of mean subtraction (MS) approach and Marsili's method [11] depend on the CFO values, whereas Lin's [9] and Xia's [10] methods are independent of CFO values. This can be explained by the fact that CFO is not estimated in the subtract mean approach and Marsili's method. On the other hand, in Lin's method CFO estimation is used for DC offset estimation. In the Xia's method, the distortion caused CFO is mitigated by using the information provided by three subcarriers -1, 0, and 1. The amount of energy leaking to DC is estimated by averaging the subcarriers -1 and 1, then subtracting them from the DC component. Therefore, the method's performance is independent of CFO. The same figure shows that the performances of the mean subtraction approach and Marsili's method degrade for

the CFO values around the center of two subcarriers's frequencies. At these CFO values, the amount of energy leaking to DC due to CFO increases as can be seen from Fig. 2.

The performance of the Marsili's method depends on the prior information about the normalized CFO parameter which is modeled as a uniform random variable in this method. In Fig. 6 (left), taking a large interval for the uniform random variable degrades the performance of the Marsili's method. When there is a strong information about CFO, the interval for the uniform random variable can be decreased which increases the performance of this method.

In Fig. 6 (right) DC offset estimation performance is investigated versus varying DC offset values. MSE remains constant for all the methods as DC offset changes.

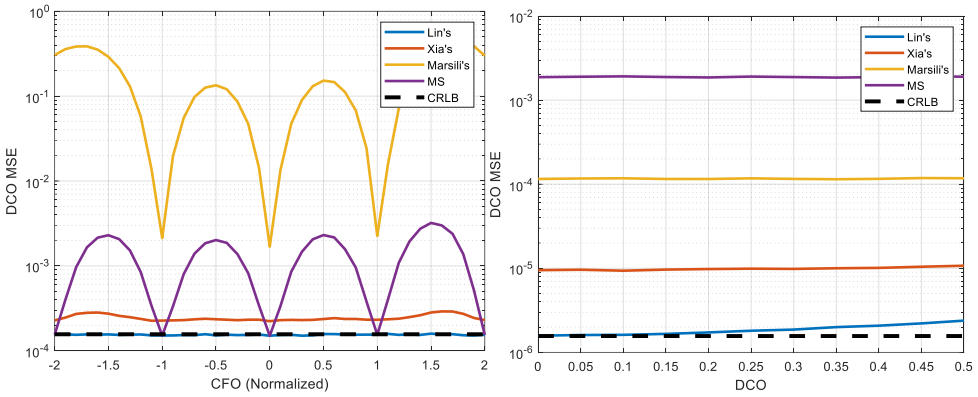

FIGURE 6. MSE of DC offset estimation versus CFO for DCO=0.1+*j*0.1 and SNR=20 dB (left). MSE of DC offset estimation versus DC offset for CFO=0.4 and SNR=40 dB (right).

DC offset estimation performance was evaluated for varying SNR levels. In these simulations, the CFO values were chosen to be 0.001 and 0.4 in order to observe the effect of CFO values on the DC offset estimation. DC offset is taken as 0.1+*j*0.1, since the value of DC offset does not change the MSE performance as seen from Fig. 6 (right). MSE of DC offset estimation for two different normalized CFO values are given in Fig. 7. Lin's method has the best estimation performance which is very close to Cramer-Rao Lower Bound (CRLB) [15] as can be seen from Fig. 6 and Fig 7. Xia's method has also a good performance for the considered SNR levels. The underlying reason for this result is that these two methods use more than one unloaded subcarriers which is a strong prior information to estimate DC offset. For the mean subtraction approach, MSE values does not decrease as the SNR level is increased above 20 dB. In this method, only DC subcarrier is used for estimation without considering CFO. In Marsili's method, the interval for normalized CFO

parameter was taken as [-1, 1]. This uncertainty limits its performance for high SNR levels.

For the low value of CFO (0.001), the amount of energy leaking to DC is substantially decreased. Therefore, performances of all the methods are increased and very close to the CRLB as seen from Fig. 7 (right). This result is consistent with the result in Fig. 6 (left). For Marsili's method, the interval for the uniform random variable was taken as [-0.1, 0.1]. Note that better performance can be obtained with this method when more specific prior information is provided.

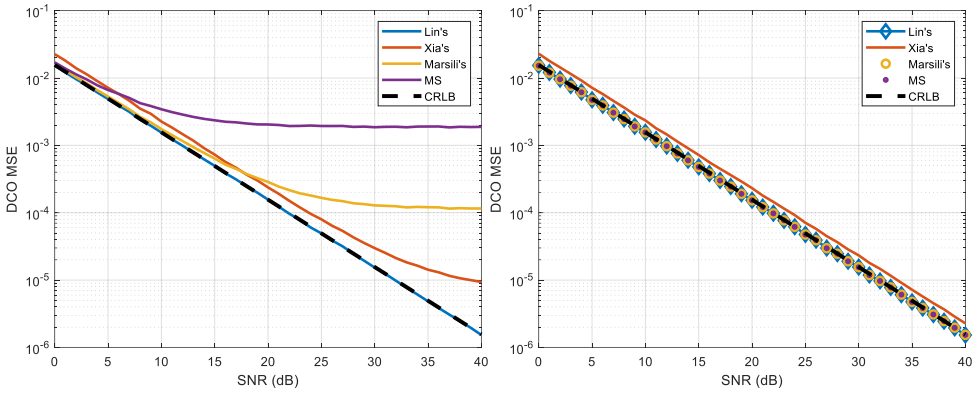

FIGURE 7. MSE of DC offset estimation versus SNR for the CFO values of 0.4 (left) and 0.001 (right) when DC offset is 0.1+*j*0.1.

6. EXPERIMENTAL RESULTS

The effect of DC offset compensation on the transmission performance in an indoor wireless channel was evaluated through experiments by using a software defined radio (SDR) including receiver and transmitter units, which is shown in Fig 8. A low resolution image was transmitted in the form of IEEE 802.11 packets through the channel and captured by the receiver antenna. Captured RF signals were downconverted to the baseband and digitized by the software defined radio. The decoding process was carried out by using the Matlab WLAN software toolbox [16]. Transmission success rate was calculated by the ratio of number of received images to the number of all transmitted images. Transmissions over the wireless channel were repeated 1000 times and transmission success rates were calculated.

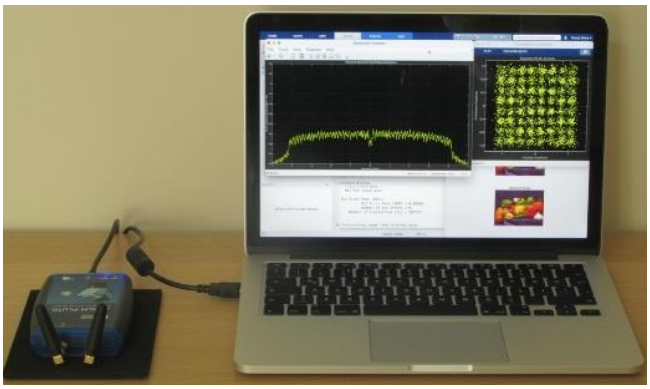

FIGURE 8. Experimental setup consisting of computer and SDR connected via USB 2.0 interface.

In the experiments, DC compensation property of the SDR was turned-off in order to implement the digital signal processing techniques considered in this paper. These methods were applied to the received signals to estimate the DC offset in WLAN packets. The transmission success rate obtained for each method is shown in Fig. 9. From this figure, it can be seen that the transmission success rate is low (23%) in the absence of DC offset compensation. Substantial performance increase was observed when the DC offset was compensated. As seen from the figure, the transmission success rate is over 70% for all the methods.

Digital signal processing methods analyzed herein except the mean subtraction (MS) approach use prior information about the non-HT transmission format such as loaded and unloaded subcarrier indices. Therefore, a better performance is expected with these methods. In this experiment, a result consistent with this expectation was obtained. The experimental performance of the methods for this experiment is similar to the performance obtained by simulations for a low CFO value in Fig 7 (right), since CFO values are low for this experimental setup. However, it should be noted that the observed performance of the methods may vary for different experimental scenarios due to the factors such as interference and multipath effects.

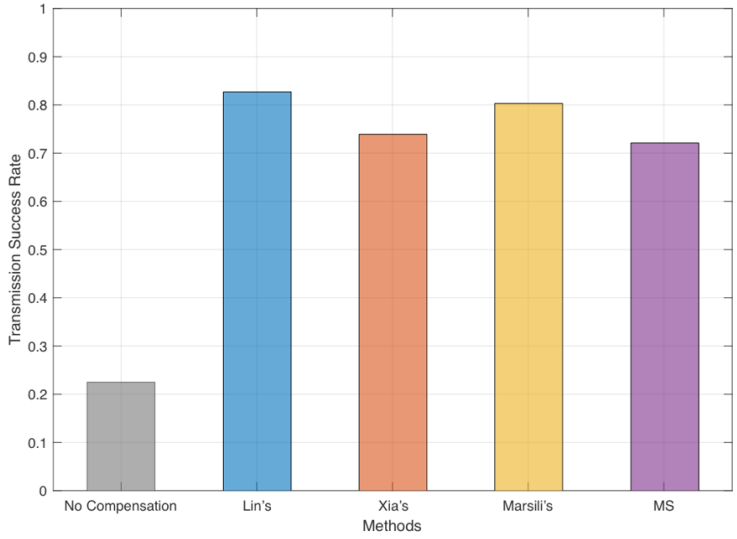

FIGURE 9. Experimental transmission success rates calculated over 1000 trials for the cases where the DC offset is uncompensated and compensated with different methods.

7. CONCLUSIONS

DC offset problem is considered in direct-conversion receivers for WLAN communication systems in this paper. The performance of the DC offset estimation methods have been compared using experimental and simulation data. It has been emphasized that DC offset and frequency offset problems should be considered together for WLAN systems. The results obtained in the paper show that the methods considering CFO values for DC offset estimation can increase the overall system performance. It has been demonstrated that the performance of the DC offset estimation methods depend on the prior information used for the estimation. In this work, data-aided methods have been analyzed for WLAN systems. Blind methods should also be considered for a network in which different wireless protocols are used.

Author Contribution Statements The authors contributed equally to this work.

Declaration of Competing Interests The authors declare that they have no known competing financial interests or personal relationships that could have appeared to influence the work reported in this paper.

Acknowledgement This work was supported by The Scientific and Technological Research Council of Turkey (TUBITAK) under Grant 119E598.

REFERENCES

[1] Bronckers, S., Roc'h, A., Smolders, B., Wireless Receiver Architectures Towards 5G: Where Are We?, *IEEE Circuits Syst. Mag.*, 17 (3) (2017), 6-16, https://doi.org/10.1109/MCAS.2017.2713306.

[2] Mirabbasi, S., Martin, K., Classical and modern receiver architectures, *IEEE Commun. Mag.*, 38 (11) (2000), 132–139, https://doi.org/10.1109/35.883502.

[3] Razavi, B., Design considerations for direct-conversion receivers, *IEEE Trans. Circuits Syst. II: Analog Digit. Signal Process.*, 44 (6) (1997), 428–435, https://doi.org/10.1109/82.592569.

[4] Abidi, A. A., Direct-conversion radio transceivers for digital communications, *IEEE J. Solid-State Circuits*, 30 (12) (1995), 186–187, https://doi.org/10.1109/4.482187.

[5] Yih, C. -H., Analysis and compensation of DC offset in OFDM systems over frequency-selective Rayleigh fading channels, *IEEE Trans. Veh. Technol.*, 58 (7) (2009), 3436–3446, https://doi.org/10.1109/TVT.2009.2014240.

[6] Xiangning, F., Yutao, S., Yangyang, F., A CMOS DC offset cancellation (DOC) circuit for PGA of low IF wireless receivers, *2010 International Symposium on Signals, Systems and Electronics*, (2010), 1-4, https://doi.org/10.1109/ISSSE.2010.5607078.

[7] Sohn, I. -H., Jeong, E. -R., Lee, Y. H., Data-aided approach to I/Q mismatch and DC offset compensation in communication receivers, *IEEE Commun. Lett.*, 6 (12) (2002), 547-549, https://doi.org/10.1109/LCOMM.2002.806451.

[8] Tseng, H. -Y., Cho, W. -J., Chang, T. -K., Phoong, S. -M., Lin, Y. -P., Compensation of IQ Imbalance and DC Offset for OFDM Transmission over Frequency Selective Channels, *2008 IEEE International Conference on Communications*, (2008), 641–645, https://doi.org/10.1109/ICC.2008.126.

[9] Lin, H., Wang, X. and Yamashita, K., A Low-Complexity Carrier Frequency Offset Estimator Independent of DC Offset, *IEEE Commun. Lett.*, 12 (7) (2008), 520-522, https://doi.org/10.1109/LCOMM.2008.080408.

[10] Xia, Y., Ren, G., A high accuracy DC offset estimation scheme for OFDM based WLAN, *2011 IEEE International Conference on Signal Processing, Communications and Computing (ICSPCC)*, (2011), 1-4, https://doi.org/10.1109/ICSPCC.2011.6061726.

[11] Marsili, S., DC offset estimation in OFDM based WLAN application, *IEEE Global Telecommunications Conference, GLOBECOM '04.*, 6 (2004), 3531–3535, https://doi.org/10.1109/GLOCOM.2004.1379023.

[12] IEEE Std. 802.11, IEEE Standard for Information Technology-Telecommunications and Information Exchange Between Systems Local and Metropolitan Area Networks-Specific Requirements Part 11: Wireless LAN Medium Access Control (MAC) and Physical Layer (PHY) Specifications, 2016.

[13] Lin, H., Sankassa, H. M., Senevirathna, B., Yamashita K., Blind Estimation of Carrier Frequency Offset and DC Offset for OFDM Systems, *IEEE Trans. Commun.*, 56 (5)

(2008), 704-707, https://doi.org/10.1109/TCOMM.2008.060215.

[14] MathWorks, https://www.mathworks.com/help/wlan/, 2022.

[15] Bar-Shalom, Y., Kirubarajan, T., Li, X. -R., Estimation with Applications to Tracking and Navigation, Wiley, New York, 2001.

[16] MathWorks, https://www.mathworks.com/help//supportpkg/plutoradio/ug/transmission and-reception-of-an-image-using-wlan-system-toolbox-and-a-single-pluto-radio.html, 2022.

http://communications.science.ankara.edu.tr

Commun.Fac.Sci.Univ.Ank.Ser. A2-A3
Volume 64, Number 1, Pages 40–50 (2022)
DOI:10.33769/aupse.1107590
ISSN 1303–6009 E-ISSN 2618–6462

Research Article; Received:April 22, 2022; Accepted: May 22, 2022

CLASSIFICATION OF FIVE DIFFERENT RICE SEEDS GROWN IN TURKEY WITH DEEP LEARNING METHODS

Bulent TUGRUL[1]
[1]Department of Computer Engineering, Ankara University, Ankara, TURKEY

Abstract. The increase in the world population and harmful environmental factors such as global warming necessitate a change in agricultural practices with the traditional method. Precision agriculture solutions offer many innovations to meet this increasing need. Using healthy, suitable and high-quality seeds is the first option that comes to mind in order to harvest more products from the fields. Seed classification is carried out in a labor-intensive manner. Due to the nature of this process, it is error-prone and also requires a high budget and time. The use of state-of-the-art methods such as Deep Learning in computer vision solutions enables the development of different applications in many areas. Rice is the most widely used grain worldwide after wheat and barley. This study aims to classify five different rice species grown in Turkey using four different Convolutional Neural Network (CNN) architectures. First, a new rice image dataset of five different species was created. Then, known and widely applied CNN architectures such as Visual Geometry Group (VGG), Residual Network (ResNet) and EfficientNets were trained and results were obtained. In addition, a new CNN architecture was designed and the results were compared with the other three architectures. The results showed that the VGG architecture generated the best accuracy value of 97%.

1. Introduction

Since cereals are a source of protein, carbohydrates and fat, they have a crucial role in continuing of human life. Rice (Oryza sativa (Asian rice) or Oryza glaberrima (African rice)), which is one of the most fundamental food sources in the world, has an essential place in the food culture of many countries, especially far eastern countries [1]. It is estimated that there are thousands of rice types grown by farmers. There are 33 registered rice species in Turkey, but only 15 of them are widely cultivated [2]. Some species have more commercial value in terms of their nutritional value, taste, appearance and structure. The most cultivated species is

Keywords. Convolutional neural networks, VGG, ResNet, EfficientNet.
btugrul@eng.ankara.edu.tr-Corresponding author
0000-0003-4719-4298.

Osmancık due to its high yield. Some other rice species produced in Turkey are Ergene, İpsala, Altınyazı, Yatkın, Cameo, Demir, Sarıkılçık and Özgür.

The commercial value of rice depends on its genetic characteristics and quality. Currently, the classification of seeds is carried out visually by experienced employees. This process, which is both laborious and slow, can cause financial losses because it cannot be done with adequate precision. Furthermore, even a skilled person can provide accurate and reliable quality control on only a few common rice varieties. If this problem can be solved with an automated process based on a computer vision system, it will provide a more accurate and stable seed classification. Thus, the incomes of both farmers and countries will increase with the increase in the quality of the crops to be harvested. Besides, the natural variety of seeds makes the process of classification with computer vision a challenging problem.

Computer vision gives computers the ability to recognize the world around them through visual inputs. Thus, the necessary actions can be taken. Basically, a computer vision system has two components. The first component is a sensing device that captures an image or video. The other is called an interpreting device that processes input and generates an output. Collaboratively, they both try to understand and interpret the objects and the events that occur around them.

Computer vision has been improving rapidly in parallel with the great developments in Artificial Intelligence (AI) and Deep Learning (DL) in recent years [3]. It finds widespread application areas in many fields, from autonomous vehicles to disease detection. Moreover, DL has reached the capability to create new things like new human faces that didn't exist before [4]. A traditional computer vision pipeline necessitates the following steps; visual data acquisition, pre-processing, feature extraction and model building. DL, on the contrary, eliminates the feature extraction phase from the traditional computer vision pipeline. DL methods can learn representations through a series of data transformations in their successive layers.

The main objective of this study is to create a new rice dataset that did not exist before and to compare the performances of various CNN architectures on this dataset. For this purpose, seeds of five different types of rice, which are widely grown and consumed in Turkey, were obtained from distinct locations. The images of the seeds were captured using a digital microscope. A database was created by randomly selecting approximately a thousand images of each type.

1.1. **Related Studies.** Before the widespread use of DL methods, the seed classification problem was solved with traditional computer vision methods. Huang and Chien extracted the shape features of rice seeds and trained the collected dataset using a Multilayer Neural Network to classify them [5]. The highest accuracy value was achieved in the Tainan-11 type with 97.35%. Ali et al. derived all morphological, texture, and color features of six different rice species and applied fuzzy logic methods [6]. According to their results, the lowest accuracy value is 94.2% and the highest value is 98.9%.

There are also numerous comparative studies using traditional machine learning and DL methods. Qui et al. captured hyperspectral images of four rice species at two different spectral ranges. KNN, SVM and CNN models were chosen as a classifier [7]. As expected, the CNN model gave the best results over the other methods. They also concluded that more accurate CNN models could be built by increasing the number of samples. Kiratiratanapruk et al. classified 14 rice varieties with four statistical machine learning methods (LR, LDA, k-NN, and SVM) and five different CNN architectures (VGG16, VGG19, Xception, InceptionV3, and InceptionResNetV2) [8]. The SVM method gives the highest accuracy value among machine learning methods with 90.61%. On the other hand, InceptionResNetV2 model produces a 95.15% accuracy value much more successful than other models.

In parallel with the developments in DL methods and technology, various CNN architectures have started to be preferred in solving the seed classification problem. Hoang et al. classified six rice types using eleven different CNN architectures [9]. DenseNet with 121 layers has a 99.05% accuracy value. Despite this, MobileNet gave the worst results, training fewer parameters than other CNN models. Gilanie et al. proposed their CNN model called RiceNet to classify Pakistani grown seven different rice seeds [10]. They also trained VGG-19, ResNet50, and GoogleNet(Inception-V3) to compare the results with their model. RiceNet has succeeded in accurately classifying all types of rice with 100% success.

2. Convolutional Neural Networks

Recent developments in Artificial Intelligence and Deep Learning have allowed computer vision systems to build more accurate and reliable classifier systems than a human can do. DL methods, such as CNN, enhance the accuracy of classification models by using a large data set and sufficient computing power. CNN consists of a variety of layers, such as input, convolution, pooling, fully connected, softmax and output. In a DL architecture, the first layer that receives raw pixels of input data learns how to represent simple features. Each successive layer learns the complex features of the previous layer as they collect and recombine the features of the previous layers. Adding more layers to the network allows it to handle higher-dimensional data.

Basically, a CNN architecture has three types of layers that can be seen in almost any model.

- Convolutional layer: Extracts features from visual inputs.
- Pooling layer: Reduces the number of parameters passed to the next layer.
- Fully connected layer: A Multi-layer Perceptron (MLP) network that takes features learned from the previous layer as input and returns class labels as output.

2.1. **Visual Geometry Group (VGG).**

Although VGG is not the winner of the 2014 ImageNet Large-Scale Visual Recognition Challenge (ILSVRC) competition,

it has been used in many applications due to its modular and simpler architecture [11]. Unlike previous CNNs, VGG prefers smaller kernel sizes. This property causes VGG to increase its expressability. VGG architecture has several different variations according to the number of layers. The smallest one (VGG-11) has 11 layers and 133 million parameters. The largest one (VGG-19) consists of 19 layers and requires 144 million parameters to be tuned. The architecture of the VGG is displayed in Figure 1.

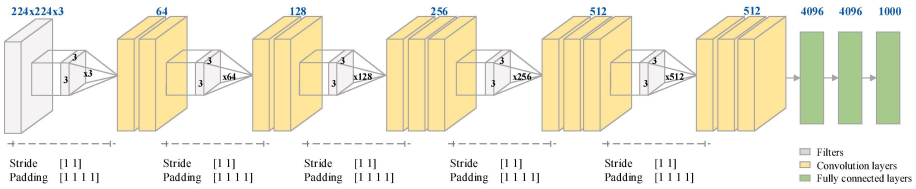

FIGURE 1. The architecture of VGG [12].

2.2. **Residual Network (ResNet).** ResNet, which won all five categories of the ImageNet Challenge in 2016, was proposed by Microsoft Research Team [13]. The top-5 error rate of ResNet is 3.57%. With the addition of more layers to deep learning models, the vanishing gradient problem arises. ResNet tackles this problem by devising a residual module with a skip connection. This approach allows them to train networks with 50, 101, and 152 layers without increasing the number of parameters.

2.3. **EfficientNets.** EffiencetNets suggests a new scaling technique that scales all dimensions using a compound coefficient [14]. Previous CNN models prefer to scale only one of the three dimensions. They designed seven different versions of the model called EffiencetNets. Top-1 accuracy of EfficientNet-B7 is 84.3% on ImageNet. They also conducted experiments using five different learning data sets, including CIFAR-100. The results show that the proposed method can perform better using fewer parameters. The architecture of EfficientNet-B0 is given in Figure 2.

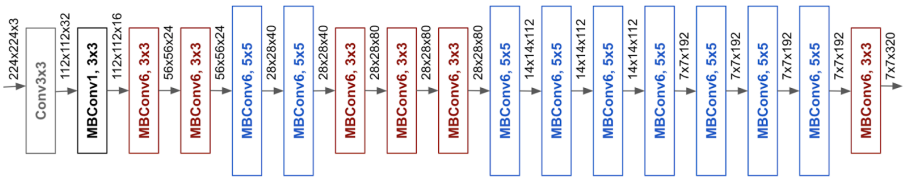

FIGURE 2. The architecture of EfficientNet-B0.

2.4. **The Custom CNN Model.** In addition to the three popular CNN architectures preferred in computer vision problems, a new CNN model was designed. The new model consists of a total of 16 layers. The first layer is the input layer used to feed the network. Images with a size of 66x64x3 will be fed through this layer. Then there are successive convolutional and pooling layers. Finally, there are the fully connected, softmax and output layers. The architecture of the custom CNN architecture is given in Figure 3. In addition, a detailed description of the custom architecture can be found in Table 1.

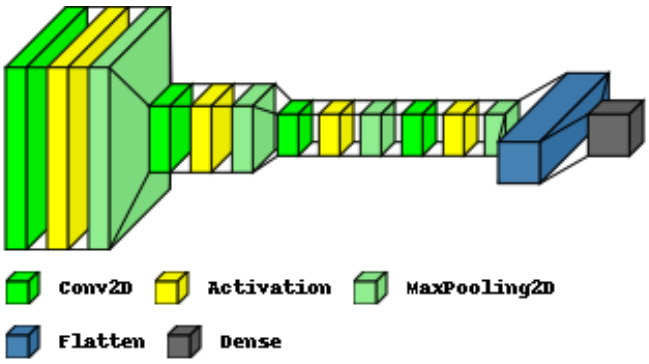

FIGURE 3. The architecture of the custom CNN model.

3. METHODOLOGY

3.1. **Image Acquisition.** The rice seed images were acquired using a digital microscope with a spatial resolution of 0.01 mm/pixel and a color depth of 24 bit. The images were captured under natural lighting conditions. There are 6833 images of Turkey's five most extensively grown rice seed species. These species are Osmancık, Cameo, Özgür, Sarıkılçık and Yatkın. Between 703 and 1736 images of each type were randomly selected to ensure that the dataset was balanced proportionately. An expert on rice seed labelled all seed images according to their class. A sample of each rice type is displayed in Figure 4.

3.2. **Performance Metrics.** The success of classification models should be evaluated using various criteria. Thus, the results of different architectures will be compared and the most successful one will be selected. Accuracy is the most common and frequently used criterion. The accuracy formula is as follows;

$$Accuracy = \frac{TP + TN}{TP + TN + FP + FN} \tag{1}$$

TABLE 1. Description of the custom CNN model.

Layer #	Operation layer		Stride value	Activation
1	Input Image			64x64x3
2	Convolutional Layer	Convolutional	3x3	22x22x64
3		ReLu		22x22x64
4	Pooling Layer	Max Pooling	1x1	22x22x64
5	Convolutional Layer	Convolutional	3x3	8x8x256
6		ReLu		8x8x256
7	Pooling Layer	Max Pooling	1x1	8x8x256
8	Convolutional Layer	Convolutional	3x3	3x3x256
9		ReLu		3x3x256
10	Pooling Layer	Max Pooling	1x1	3x3x256
11	Convolutional Layer	Convolutional	3x3	1x1x256
12		ReLu		1x1x256
13	Pooling Layer	Max Pooling	1x1	1x1x256
14	Inner Product Layer	Fully Connected		1x1x5
15	Softmax Layer	Softmax		1x1x5
16	Classification Layer	Classification Output		5

TABLE 2. Description of rice seed image dataset.

Rice Species	Number of Images
Cameo	1736
Osmancık	1246
Özgür	703
Sarıkılçık	1456
Yatkın	1692

Accuracy alone is not a sufficient criterion in some special cases. In addition, Precision and Recall values are also preferred to evaluate the performance and robustness of classification models. F1-Score is the geometric mean of both Precision and Recall.

$$Precision = \frac{TP}{TP + FP} \tag{2}$$

$$Recall = \frac{TP}{TP + FN} \tag{3}$$

$$F1 - Score = \frac{2 * Precision * Recall}{Precision + Recall} = \frac{2 * TP}{2 * TP + FP + FN} \tag{4}$$

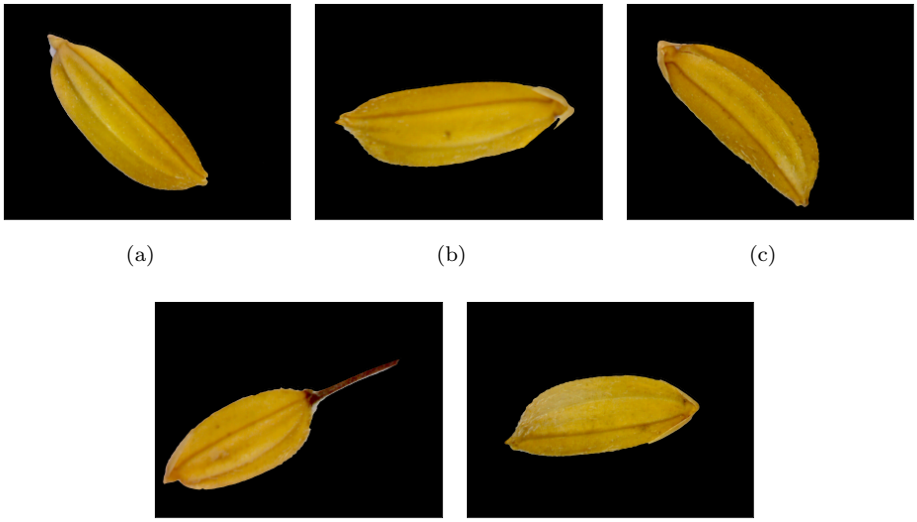

(a) (b) (c)

(d) (e)

FIGURE 4. Sample images of different species of *Rice* (a) *Cameo* (b) *Osmancık* (c) *Özgür* (d) *Sarıkılçık* (e) *Yatkın*.

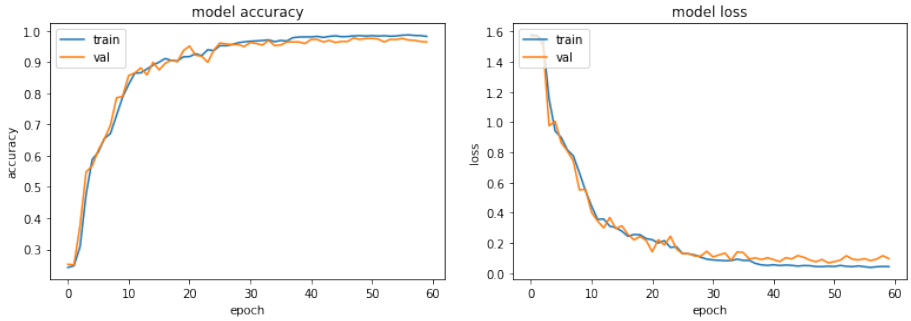

(a) (b)

FIGURE 5. VGG.

4. Results and Discussion

Classification of rice seeds is carried out by traditional methods that require heavy human labor. However, rice seed types are very similar in terms of shape, texture and color, so the probability of making mistakes is high. Recently, many studies

have been published showing that DL methods successfully classify different types of seeds. For this purpose, an image data set of five different species grown in Turkey was created. This dataset was trained with three different popular and custom CNN architecture. The accuracy and loss graphics of each CNN architecture's training and validation data are displayed in Figures 5 , 6, 7 and 8. The confusion matrix and overall performance of the CNN models are presented in Tables 3 and 4, respectively.

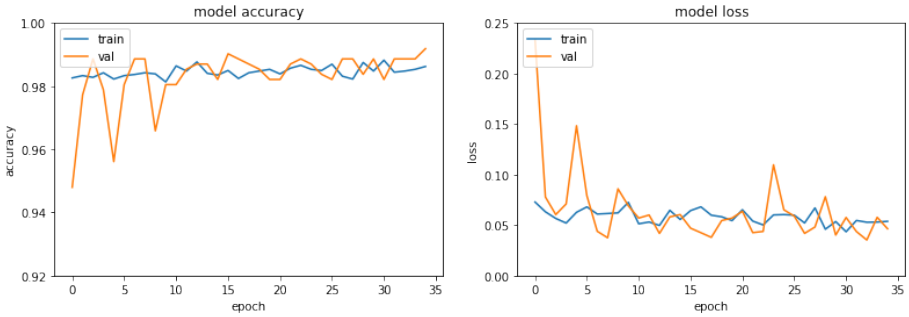

(a) (b)

FIGURE 6. ResNet.

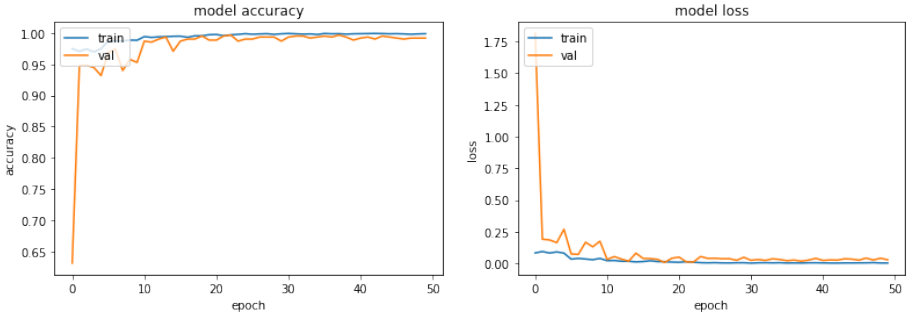

(a) (b)

FIGURE 7. EfficientNet.

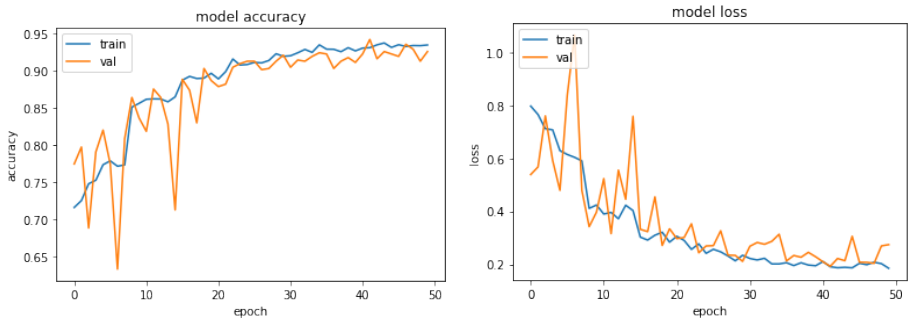

(a) (b)

FIGURE 8. The Custom CNN model.

TABLE 3. Confusion matrix of CNN architectures.

Rice Species	CNN Architectures	Cameo	Osmancık	Özgür	Sarıkılçık	Yatkın
Cameo	VGG	165	0	1	0	3
	ResNet	169	0	0	0	0
	Efficient	168	0	0	1	0
	Custom	159	0	0	4	6
Osmancık	VGG	0	128	2	0	0
	ResNet	1	113	16	0	0
	Efficient	0	97	33	0	0
	Custom	0	127	3	0	0
Özgür	VGG	0	2	63	1	0
	ResNet	7	0	59	0	0
	Efficient	2	0	63	1	0
	Custom	3	2	59	2	0
Sarıkılçık	VGG	0	0	0	145	0
	ResNet	8	0	0	137	0
	Efficient	1	0	0	144	0
	Custom	0	0	0	145	0
Yatkın	VGG	9	0	0	0	165
	ResNet	41	0	0	0	133
	Efficient	84	0	0	0	90
	Custom	8	0	0	0	166

TABLE 4. Overall performance of CNN architectures.

CNN Architectures	Accuracy	Precision	Recall	F1-Score
VGG	0.97	0.97	0.97	0.97
ResNet	0.89	0.91	0.89	0.89
EfficientNet	0.82	0.88	0.82	0.82
Custom	0.96	0.96	0.96	0.96

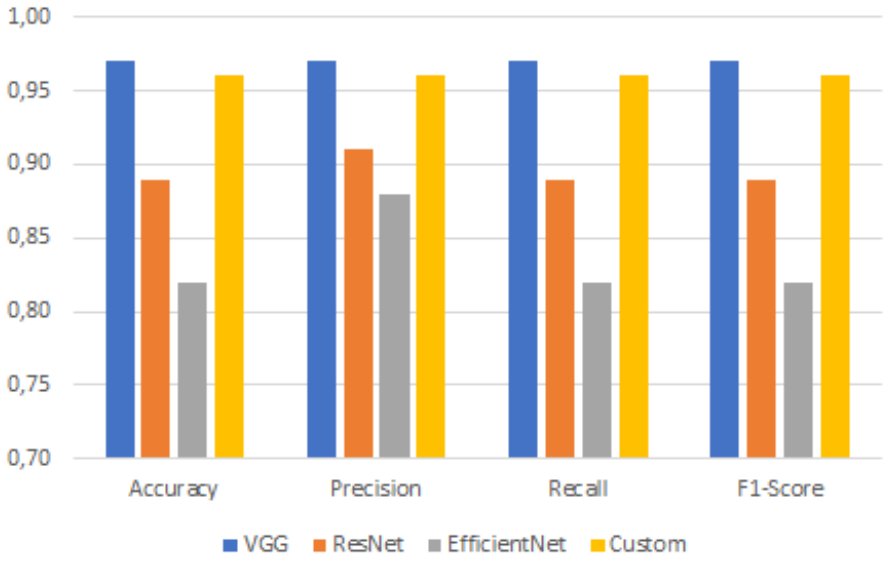

FIGURE 9. Overall performance of CNN architectures.

As shown from Tables 3 and 4, VGG and the custom CNN architecture generated successful and robust results. The best performance belongs to VGG and has an accuracy value of 0.97. The custom model is more successful than both ResNet and EfficientNet. Even though it is worse than VGG, its performance is promising as a classifier.

5. Conclusions and Future Works

The main objective of this study is to classify the rice seeds data set with three different and a new custom CNN architecture. For this purpose, a data set consisting of five different types of rice grown in Turkey was created. According to the results, it was observed that the CNN architecture with the best accuracy value was VGG. The other architectures have also generated acceptably close results. Thus, it was shown that the classification of rice seeds could be carried out more successfully with advanced computer vision methods. This study used only images of five different seed types and four different CNN architectures. In future studies, we aim to broaden the data set by increasing both the number of images and the number of rice species. We also plan to get results using the Vision Transformers (ViT).

Declaration of Competing Interests The author declare that he has no known competing financial interests or personal relationships that could have appeared to influence the work reported in this paper.

References

[1] Chen, C., He, W., Nassirou, T. Y., Nsabiyumva, A., Dong, X., Adedze, Y. M. N., Jin, D., Molecular characterization and genetic diversity of different genotypes of Oryza sativa and Oryza glaberrima, *Electron. J. Biotechnol.*, 30 (2017), 48–57, https://doi.org/10.1016/j.ejbt.2017.08.001.

[2] Taşlıgil, N., Şahin, G., Türkiye'de çeltik (Oryza sativa L.) yetiştiriciliği ve coğrafi dağılımı, *Adıyaman Üniversitesi Sosyal Bilimler Enstitüsü Dergisi*, 6 (2011), 182–203, https://doi.org/10.14520/adyusbd.105.

[3] Voulodimos, A., Doulamis, N., Doulamis, A., Protopapadakis, E., Deep learning for computer vision: A brief review, *Comput. Intell. Neurosci.*, 2018 (2018), https://doi.org/10.1155/2018/7068349.

[4] Creswell, A., White, T., Dumoulin, V., Arulkumaran, K., Sengupta, B., Bharath, A. A., Generative adversarial networks: An overview, *IEEE Signal Process Mag.*, 35 (1) (2018), 53–65, https://doi.org/10.1109/MSP.2017.2765202.

[5] Huang, K., Chien, M., A novel method of identifying paddy seed varieties, *Sensors*, 17 (4) (2017), 809–816, https://doi.org/10.3390/s17040809.

[6] Ali, T., Jhandhir, Z., Ahmad, A., Khan, M., Khan, A. A., Choi, G. S., Detecting fraudulent labeling of rice samples using computer vision and fuzzy knowledge, *Multimed. Tools Appl.*, 76 (23) (2017), 24675–24704, https://doi.org/10.1007/s11042-017-4472-9.

[7] Qiu, Z., Chen, J., Zhao, Y., Zhu, S., He, Y., Zhang, C.,, Variety identification of single rice seed using hyperspectral imaging combined with convolutional neural networks, *Appl. Sci.*, 8 (2) (2018), 212–223, https://doi.org/10.3390/app8020212.

[8] Kiratiratanapruk, K., Temniranrat, P., Sinthupinyo, W., Prempree, P., Chaitavon, K., Porntheeraphat, S., Prasertsak, A., Development of paddy rice seed classification process using machine learning techniques for automatic grading machine, *J. Sens.*, 2020 (2020), https://doi.org/10.1155/2020/7041310.

[9] Hoang, V. T., Van Hoai, D. P., Surinwarangkoon, T., Duong, H. T., Meethongjan, K., A comparative study of rice variety classification based on deep learning and hand-crafted features, *ECTI Transactions on Computer and Information Technology (ECTI-CIT)*, 14 (1) (2020), 1–10, https://doi.org/10.37936/ecti-cit.2020141.204170.

[10] Gilanie, G., Nasir, N., Bajwa, U. I., Ullah, H., RiceNet: Convolutional neural networks-based model to classify Pakistani grown rice seed types, *Multimed. Syst.*, 27 (5) (2021), 867–875, https://doi.org/10.1007/s00530-021-00760-2.

[11] Simonyan, K., Zisserman, A., Very deep convolutional networks for large-scale image recognition, *arXiv preprint arXiv:1409.1556*, (2014), https://doi.org/10.48550/arXiv.1409.1556.

[12] Altuntaş, Y., Cömert, Z. Kocamaz, A. F., Identification of haploid and diploid maize seeds using convolutional neural networks and a transfer learning approach, *Comput. Electron. Agric.*, 163 (2019), 104874, https://doi.org/10.1016/j.compag.2019.104874.

[13] He, K., Zhang, X., Ren, S., Sun, J., Deep residual learning for image recognition, *Proceedings of the IEEE conference on computer vision and pattern recognition*, (2016), 770–778.

[14] Tan, M., Le, Q., Efficientnet: Rethinking model scaling for convolutional neural networks, *International conference on machine learning*, (2019), 6105–6114.

http://communications.science.ankara.edu.tr

Commun.Fac.Sci.Univ.Ank.Ser. A2-A3
Volume 64, Number 1, Pages 51–65 (2022)
DOI:10.33769/aupse.1100013
ISSN 1303–6009 E-ISSN 2618–6462

Review Article; Received: April 07, 2022; Accepted: May 16, 2022

AVERAGES OF OBSERVABLES ON GAMOW STATES

Manuel GADELLA[1] and Carlos SAN MILLAN[1]

[1]Departamento de Física Teórica, Atómica y Optica and IMUVA,
Universidad de Valladolid, Valladolid, SPAIN

Abstract. We propose a formulation of Gamow states, which is the part of unstable quantum states that decays exponentially, with two advantages in relation with the usual formulation of the same concept using Gamow vectors. The first advantage is that this formulation shows that Gamow states cannot be pure states, so that they may have a non-zero entropy. The second is the possibility of correctly defining averages of observables on Gamow states.

1. Introduction

Textbooks in Quantum Mechanics mostly deal with the so called bound states, which are described by eigenvectors (in explicit models, eigenfunctions) of a given Hamiltonian, H. Bound states are invariant under the time evolution governed by H. Thus, bound states are stable states, unless that are exposed to interactions with new external forces.

However, a substantial amount of quantum systems really existing in Nature are unstable. The range of unstable quantum systems include excited atoms, nuclei and particularly elementary particles. Needless to say that a Quantum Theory for unstable quantum states has been developed [1–5], although it may be considered as incomplete for various reasons, some of them will be the object of our study in the present paper.

Unstable quantum systems have historically received different names: quasi-stable states, meta-stable states, scattering resonances, etc, which have received different definitions, but that all have been proven to be the same. They have a common feature: they have an experimental exponential decay at *most* observable times. We have underlined the word *most*, since the ranges of time for which this decay is not exponential are very difficult to observe in practice. These deviations that have been foreseen by the general theory [5, 6] have been observed for very short [7] or very high times [8]. Nevertheless, the observed exponential decay for

Keywords. Quantum resonances, Gamow states, algebraic formulation of states and observables.

manuelgadella1@gmail.com-Corresponding author; carlos.san-millan@alumnos.uva.es
0000-0001-8860-990X; 0000-0001-7506-5552.

most times is not exact due to noise [5]. Thus, exponential decay may be considered as a very good approximation for the behaviour of quantum unstable systems for most purposes.

Generally speaking, quantum unstable states, henceforth *resonances*, are produced in resonance scattering [1] due to the presence of some external forces, which are usually given by a potential V. A particle, otherwise looked as free, evolves under the free dynamics given by H_0 up to it enters on the region where the interaction of V takes place. Then, the particle finally escapes from this interaction. If this particle stays in the interaction region a much higher time it would have stayed should this interaction not exist, we say that a resonance has been produced. Thus, for the creation of a scattering resonance, we need a Hamiltonian pair, $\{H_0, H\}$, where $H = H_0 + V$, V being the potential responsible for the creation of the resonance. Typically, point potentials [10] give often resonances.

Resonances are characterized in various forms from the physical point of view, not always equivalent [1]. Possibly the most popular among the physicists is given by poles of the analytic continuation of the scattering function (or matrix) $S(k)$ in representation of momenta. These poles are located on the lower half plane and appear in pairs symmetric to the negative imaginary axis. If instead of this representation, we go to energies, resonance poles are pairs of conjugate complex numbers located on the analytic continuation of $S(E)$ through the cut given by the spectrum of the total Hamiltonian H, and these poles lie on the second sheet of the Riemann surface associated to the transformation $k = \sqrt{2mE}$. Each pair of resonance poles have the form $E_R \pm i\Gamma/2$ with $E_R, \Gamma > 0$.

Is it possible to define a vector state for a unstable quantum state as is for a bound state? The vector state, ψ, for an unstable quantum state should have the following property: its probability amplitude in terms of time, t, which is given by

$$\alpha(t) := \langle \psi | e^{-itH} | \psi \rangle \,, \tag{1}$$

where $H = H_0 + V$, must be approximately exponential for almost all times, with the exception of very short or very long times, which may be unobservable in most cases.

Due to this condition, Nakanishi [9] in 1959 proposed to define the vector state for a resonance as an eigenvector of the Hamiltonian with complex eigenvalues. For instance, if a resonance pole is located at the point $z_R = E_R - i\Gamma_R/2$, this vector state, $|\psi\rangle$, should be characterized by the property:

$$H \, |\psi^D\rangle = z_R \, |\psi^D\rangle = (E_R - i\Gamma_R/2) \, |\psi^D\rangle \,, \tag{2}$$

since then if t means time, formally:

$$e^{-itH} \, |\psi^D\rangle = e^{-itE_R} \, e^{-t\Gamma/2} \, |\psi^D\rangle \,, \tag{3}$$

so that the time evolution for $t \longmapsto \infty$ is a decaying exponential.

Some important comments:

i.) Each resonance is given by a pair of complex conjugate poles, so that along $|\psi^D\rangle$ it must exist another vector, $|\psi^G\rangle$, so that

$$H\,|\psi^G\rangle = z_R^*\,|\psi^G\rangle = (E_R + i\Gamma_R/2)\,|\psi^G\rangle \Longrightarrow e^{-itH}\,|\psi^G\rangle = e^{-itE_R}\,e^{+t\Gamma/2}\,|\psi^G\rangle\,. \quad (4)$$

Consequently, the vector $|\psi^G\rangle$ grows exponentially as $t \longmapsto \infty$. The superindices D and G stand precisely for *decaying* and *growing*, respectively. Note that the time behaviour of $|\psi^D\rangle$ and $|\psi^G\rangle$ as $t \longmapsto -\infty$ is the opposite.

ii.) This opposite time behaviour of the vectors $|\psi^D\rangle$ and $|\psi^G\rangle$ suggests that they may be defined as the time reverse of each other. This is exactly what happens in [11]. Both vectors represent equally well the state of one unique and the same resonance, given by the poles $z_R = E_R - i\Gamma_R/2$ and $z_R^* = E_R + i\Gamma/2$. The real part E_R is called the *resonance energy* and the imaginary part is proportional to the inverse of the mean life.

iii.) The vectors $|\psi^D\rangle$ and $|\psi^G\rangle$ are called the *decaying Gamow vector* and the *growing Gamow vector*. Decaying and growing always with reference to the *future* of increasing times.

iv.) Realistic vector states for resonances show deviations of exponential law for very small and very large values of time. At the same time the time interval with exponential decay always shows certain amount of noise, so that this exponential is usually not exact. Thus, if $|\psi\rangle$ is the vector state for a resonance, it must be a sum of two contributions:

$$|\psi\rangle = |\psi^D\rangle + |\psi^{\rm BACK}\rangle = |\psi^G\rangle + |\psi^{\rm BACK^*}\rangle\,, \quad (5)$$

so that we have split $|\psi\rangle$ into the sum of the Gamow vector plus the vector state of a certain *background*, which is a vector state including all possible effects so that diverts $|\psi\rangle$ from the purely exponential behaviour. The effect of the background vector is much smaller than the effect of the Gamow vector for the effectively observable time interval.

v.) This is the most important point. Since H is a self adjoint operator, how is it possible that it shows complex eigenvalues? Not as an operator on Hilbert space! We need to extend the Hilbert space as well as H to a larger space on which H may have complex eigenvalues.

This extension comes after the rigging of the Hilbert space of states, $\mathcal{H}$, with another two spaces, so as to make a triplet of spaces,

$$\Phi \subset \mathcal{H} \subset \Phi^\times\,, \quad (6)$$

where:

i.) The Hilbert space $\mathcal{H}$ is infinite dimensional, usually of the type of space of square integrable functions such as $L^2(\mathbb{R})$. If the space were finite dimensional a

construction like (6) would not be possible unless the other two spaces were equal to $\mathcal{H}$.

ii.) The space Φ is a dense subspace of $\mathcal{H}$. Dense means that for any $\psi \in \mathcal{H}$ and any $\varepsilon > 0$, there exists a $\phi \in \Phi$ such that $||\phi - \psi|| < \varepsilon$, where $||-||$ is the Hilbert norm ($||\psi||^2 = \langle \psi|\psi\rangle$, where $\langle -|-\rangle$ is the scalar product on the Hilbert space). In addition, it has a topology which is strictly finer than the Hilbert topology. Finer means that it has more open sets. In general, although not always, this topology is constructed with a countably infinite set of norms [12], one of which is the Hilbert space norm. This implies in particular that the canonical injection:

$$i : \Phi \longmapsto \mathcal{H}\,, \quad i(\phi) = \phi\,, \quad \forall \phi \in \Phi\,, \tag{7}$$

is continuous.

iii.) A continuous anti-linear functional, or in short, a functional on Φ is a mapping $F : \Phi \longmapsto \mathbb{C}$, where $\mathbb{C}$ is the field of complex numbers with its usual topology, such that

a) F is anti-linear:

$$F(\alpha\,\psi + \beta\,\varphi) = \alpha^*\,F(\psi) + \beta^*\,F(\varphi)\,, \quad \forall\,\alpha, \beta \in \mathbb{C}\,, \quad \forall\,\psi, \varphi \in \Phi\,. \tag{8}$$

where the star denotes complex conjugation.

b) F is continuous with the topologies on Φ and $\mathbb{C}$. Since we have not given details on the topology on Φ, we cannot give details on some properties of F. Let us call $\Phi^\times$ to the set of functionals on Φ. It forms a vector space over the complex field. The sum of functionals and the multiplication of functionals by complex numbers is given by

$$(\alpha\,F + \beta\,G)(\varphi) := \alpha\,F(\varphi) + \beta\,G(\varphi)\,, \quad \forall\,\alpha, \beta \in \mathbb{C}\,, \quad \forall\,F, G \in \Phi^\times\,, \tag{9}$$

so that $\Phi^\times$ is a linear space over the complex field.

We can endow $\Phi^\times$ with a topology compatible with the topology on Φ [13]. Each vector $\psi \in \mathcal{H}$ determines a unique functional F_ψ by $F_\psi(\varphi) := \langle \varphi|\psi\rangle$ (we take the anti-linear part of the scalar product at the left). By an *abus de langage*, we may identify F_ψ with ψ. With this idea in mind, the canonical mapping $i : \mathcal{H} \longmapsto \Phi^\times$ is one to one (and also continuous).

iv.) We call the structure (6) with all the above defined properties, a *rigged Hilbert space* (RHS) or a *Gelfand triplet* [14–29].

Next, let H be a self adjoint Hamiltonian with domain with domain $\mathcal{D} \subset \mathcal{H}$, dense in the (separable) infinite dimensional Hilbert space $\mathcal{H}$. Assume that we have a RHS like (6), with $\Phi \subset \mathcal{D}$ and $H\Phi \subset \Phi$. This means that for each $\varphi \in \Phi$, $H\varphi \in \Phi$. Then, H may be extended to a unique operator into $\Phi^\times$, that we also call H for simplicity in the notation, using the following *duality formula*:

$$\langle F|H\varphi\rangle = \langle HF|\varphi\rangle\,, \qquad \forall\,\varphi \in \Phi\,. \tag{10}$$

This duality formula defines HF for each $F \in \Phi^\times$. The operator H defined on $\Phi^\times$ by (10) is linear. Its restriction to Φ coincides with the original operator, as can be easily seen from (10). Moreover, if we assume that H is continuous on Φ, its extension by (10) is continuous on $\Phi^\times$ with all topology on this space compatible with the topology on Φ [13].

In [30–32], we have obtain a pair of RHS where the Gamow vectors are well defined as functionals and verify properties (3-4). In addition, we may define RHS so that the time evolution of the decaying Gamow vector $|\psi^D\rangle$ given by (3) be properly given for $t > 0$ only [31,32] and the time evolution of $|\psi^G\rangle$ given for $t < 0$, only. This clarifies further the meaning of the indices *Decaying* and *Growing* given to these vectors.

Once we have clarified the notion of Gamow vectors, we ask ourselves whether these vectors behave as ordinary state vectors, so that they may give expectation values of observables. A first attempt was given by Berggren [33, 34]. A possible definition of the energy average on Gamow vectors was given in [35]. None of these results were convincing. Berggren averages were intended to be used with many observables, although the average for the energy on a Gamow state was not what our intuition would say it is (the real part of the resonance pole, or resonance energy) and was rather sophisticated. The solution given in [35] was valid just for H and could not be applied to other observables, even for H^2, the square of the Hamiltonian. In summary, expressions like $\langle\psi^D|O|\psi^D\rangle$ for a given observable O are not defined. Even $\langle\psi^D|\psi^D\rangle$ does not admit a natural definition.

In the more widespread formulation of quantum mechanics, pure states are represented by vector states. The most popular representation for quantum unstable states is given by the Gamow vectors, which may suggest that Gamow states are pure states. Is this correct? This argument has two contradictions. The former is of mathematical nature. Pure states are represented by square integrable functions or normalizable vectors on a Hilbert space, which is not the case for Gamow vectors. Second, Gamow vectors somehow represent dissipative states which cannot have zero entropy. Pure states have zero entropy. The entropy for unstable quantum states via Gamow vectors have been investigated [36, 37] and certainly, it is not zero.

The generalization of all of the above to systems with N resonances is obvious. Although many models exhibit an infinite number of resonances, one may always keep a finite number since those resonances with large values of Γ_R are practically unobservable, since Γ_R is related to the inverse of the mean life. Note that poles of a meromorphic function (analytic except poles) are always isolated points.

In the present review paper, we show that Gamow states are not pure states and suggest a receipt to obtain mean values of observables on Gamow states. To this end, we have proposed a formalism based on the notion of a state as a functional over an algebra of operators including relevant observables. This construction is the objective of the next Section.

2. The Algebra of Observables and the States

Let us make the simplest possible assumptions for the Hamiltonian pair that produces a resonance phenomena, $\{H_0, H = H_0 + V\}$. For instance that both H_0 and H have a simple (non-degenerate) absolutely continuous spectrum coinciding to $[0, \infty)$. Since Hamiltonians are always semi-bounded, the choice of the spectrum as $[0, \infty)$ may be done without restriction to generality. We also assume some scattering properties like the existence of the Møller wave operators and asymptotic completeness [38, 39]. The Møller wave operators, Ω^- and Ω^+, relate the free incoming and outgoing free states with the incoming and outgoing perturbed states, respectively.

For the moment, let us focus our attention to the free Hamiltonian H_0. According to a Theorem by Gelfand and Maurin [40, 41], and under the above working hypothesis, there exists a RHS like (6) such that, i.) $H_0\Phi \subset \Phi$ and H_0 is continuous on Φ, so that H_0 may be continuously extended to the anti-dual $\Phi^\times$; ii.) For each $E \in [0, \infty)$ there exists a functional $|E\rangle \in \Phi^\times$ such that $H_0 |E\rangle = E |E\rangle$; iii.) For all $\varphi, \psi \in \Phi$, one has the following spectral decompositions:

$$\langle\varphi|H_0\psi\rangle = \int_0^\infty E \langle\varphi|E\rangle\langle E|\psi\rangle \, dE \,, \tag{11}$$

which may be written, by omitting the arbitrary $\varphi, \psi \in \Phi$ as

$$H_0 = \int_0^\infty E \, |E\rangle\langle E| \, dE \,. \tag{12}$$

It is also valid that

$$H_0^n = \int_0^\infty E^n \, |E\rangle\langle E| \, dE \,, \qquad n = 0, 1, 2, \dots \,. \tag{13}$$

Note that for $n = 0$, we have a spectral decomposition of the identity. After the aforementioned hypothesis, we have that $H = \Omega^\pm \, H_0 \, (\Omega^\pm)^\dagger$, where the dagger means the adjoint. Using a new couple of RHS, where we define the spaces $\Phi^\pm := \Omega^\pm \, \Phi$, we may consider the functionals $|E^\pm\rangle := \Omega^\pm \, |E\rangle$ in $(\Phi^\pm)^\times$. Then, $H|E^\pm\rangle = E \, |E^\pm\rangle$ and one has the following spectral decompositions for H^n, $n = 0, 1, 2, \dots$:

$$H^n = \int_0^\infty E^n \, |E^\pm\rangle\langle E^\pm| \, dE \,. \tag{14}$$

Again for $n = 0$, we have two distinct spectral decompositions for the identity, which are different from those given in (13). As a matter of fact, n could have been any real number. The above kets, $|E\rangle \,, |E^\pm\rangle$, satisfy the following product relations [42]:

$$\langle E|E'\rangle = \delta(E - E') \,, \qquad \langle E^\pm|E'^\pm\rangle = \delta(E - E') \,. \tag{15}$$

Now, we say that the operators $O^{\pm}$ are *compatible* with H if they satisfy the following spectral decompositions:

$$O^{\pm} = \int_0^{\infty} dE\, O(E)\, |E^{\pm}\rangle\langle E^{\pm}| + \int_0^{\infty} dE \int_0^{\infty} dE"\, O(E,E')|E^{\pm}\rangle\langle E'^{\pm}|$$

$$= \int_0^{\infty} dE\, O(E)\, \Omega^{\pm}|E\rangle\langle E|(\Omega^{\pm})^{\dagger} + \int_0^{\infty} dE \int_0^{\infty} dE"\, O(E,E')\Omega^{\pm}|E\rangle\langle E'|(\Omega^{\pm})^{\dagger}\,, \quad (16)$$

where $O(E)$ and $O(E,E')$ belong to certain spaces of test functions. The functions $O(E,E')$ should admit analytic continuation to analytic functions on both variables separately. Test functions should form linear spaces, which implies that the operators of the form (16) built two different linear spaces, one for $+$ and the other for $-$. In addition, we assume that the spaces of test functions $O(E)$ and $O(E,E')$ form respective algebras, which include the particular cases of $O(E) = E^n$, $n = 0, 1, 2, \ldots$ and $O(E,E') = 0$, which give respective spectral decompositions of powers of the Hamiltonian H. Then, the product of two operators is given by

$$O_1^{\pm}\, O_2^{\pm} = \int_0^{\infty} dE\, O_1(E)\, O_2(E)\, |E^{\pm}\rangle\langle E^{\pm}|$$

$$+ \int_0^{\infty} dE \int_0^{\infty} dE'\, O_1(E,E')\, O_2(E,E')\, |E^{\pm}\rangle\langle E'^{\pm}|\,. \quad (17)$$

Thus, we have two algebras of operators with identity that we represent as $\mathcal{A}^{\pm}$. These algebras are isomorphic. They have a topology induced by the topology of the algebras of test functions $O(E)$ and $O(E,E')$, although we will not insist on this particular point.

It is convenient to simplify the notation. To this end, let us introduce the following symbols:

$$|E^{\pm}) := |E^{\pm}\rangle\langle E^{\pm}|\,, \qquad |EE'^{\pm}) := |E^{\pm}\rangle\langle E'^{\pm}|\,. \quad (18)$$

With this convention, the operators in (16) are written as

$$O^{\pm} = \int_0^{\infty} O(E)\, |E^{\pm})\, dE + \int_0^{\infty} dE \int_0^{\infty} dE'\, O(E,E')\, |EE'^{\pm})\,. \quad (19)$$

In addition, we have some formal relations or "products" such that

$$(E^{\pm}|w^{\pm}) = \delta(E-w)\,, \quad (EE'^{\pm}|ww'^{\pm}) = \delta(E-w)\delta(E'-w')\,,$$

$$(EE'^{\pm}|w) = (w|EE'^{\pm}) = 0\,. \quad (20)$$

These relations permit to perform operations such as that in (17). With this notation, we may write the functions $O(E)$ and $O(E,E')$ as a sort of products such as

$$(E^{\pm}|O^{\pm}) = O(E)\,, \qquad (EE'^{\pm}|O^{\pm}) = O(E,E')\,. \tag{21}$$

The algebras $\mathcal{A}^{\pm}$ have respective identities

$$I^{\pm} := \int_0^{\infty} dE\,|E^{\pm})\,. \tag{22}$$

In addition, these algebras have an involution. It is natural to define the adjoints of the operators $O^{\pm}$ as

$$(O^{\pm})^{\dagger} = \int_0^{\infty} dE\,O^*(E)\,|E^{\pm}) + \int_0^{\infty} dE \int_0^{\infty} dE'\,O^*(E',E)\,|EE'^{\pm})\,. \tag{23}$$

As always, the star denotes complex conjugation. Observe on the transposition of variables on the function under the double integral in (23). Clearly, (23) defines respective involutions on $\mathcal{A}^{\pm}$.

Operators of the form (16) (or analogously (19)) and (23) are linear mappings $\Phi^{\pm} \longmapsto (\Phi^{\pm})^{\times}$, which are, in addition, continuous. The proof of this continuity requieres a detailed contruction of the topologies and, therefore, lies outside the scope of the present article. Observe that definition (17) allows for the definition of a product of operators and, therefore, for the structure of algebra on $\mathcal{A}^{\pm}$.

2.1. **Functionals Over the Algebras.** The algebras $\mathcal{A}^{\pm}$ are endowed with a topology compatible with the structure of algebra, which depend on the topological structure of the algebras of test functions $O(E)$ and $O(E,E')$. Functionals, $\rho^{\pm}$, over these algebras are continuous linear mappings $\rho^{\pm} : \mathcal{A}^{\pm} \longmapsto \mathbb{C}$. In the present situation, these functionals should be written in the following form:

$$\rho^{\pm} := \int_0^{\infty} dE\,\rho(E)\,(E^{\pm}| + \int_0^{\infty} dE \int_0^{\infty} dE'\rho(E,E')\,(EE'^{\pm}|\,. \tag{24}$$

Here, $\rho(E)$ is a functional (or a generalized function in the sense of Gelfand [12]) over the space of functions $O(E)$ and $\rho(E,E')$ is a functional over the space of functions $O(E,E')$. We should not forget that these functions form spaces of test functions, which have their corresponding spaces of functionals defined as usual. The action of (24) on (16) after (21) is

$$(\rho^{\pm}|O^{\pm}) = \int_0^{\infty} dE\,\rho(E)\,O(E) + \int_0^{\infty} dE \int_0^{\infty} dE'\,\rho(E,E')\,O(E,E')\,. \tag{25}$$

The meaning of the integrals in (25) should be clear as the action of the generalized functions on the test functions. Thus, the first term of the right hand side of (25) represents the action of the functional $\rho(E)$ on the function $O(E)$. Similarly,

the second. These are truly integrals if $\rho(E)$ and $\rho(E, E')$ are functions on a given space such that both integrals converge. The action of a functional, which does not admit a representation as a regular function may be exemplified taken for instance $\rho(E) = \delta(w-E)$, where this delta is the Dirac delta. Note that $(E^{\pm}|$ are functionals such that

$$\rho(E) = \delta(E - w)\,, \quad \text{and} \quad \rho(E, E') \equiv 0\,. \tag{26}$$

Analogously, the symbols $(EE'^{\pm}|$ denote the following functionals:

$$\rho(E) \equiv 0\,, \quad \text{and} \quad \rho(E, E') = \delta(E - w)\delta(E' - w')\,. \tag{27}$$

In both cases, w and w' are variables and E and E' are fixed positive real numbers.

Just a brief comment on the spaces of functions $O(E, E')$. For reasons to be understood next, these functions should be analytically continuable for each variable independently, preferable to the whole complex plane. The construction relies on some results of Mathematical Analysis that we do not want to mention here, since we do not want to involve the reader with mathematical details that, although important, distract from the objective of this presentation. They will be published in a forthcoming paper [43].

2.2. **On Quantum States.** Possibly, the most general definition of state in non-relativistic Quantum Mechanics is given by the consideration of states and observables in its algebraic formulation [44, 45]. Let us define the notion of state in this context.

The point of departure is an algebra of operators, $\mathcal{A}$, with a topology, identity, I, and an involution $O \longmapsto O^{\dagger}$ for all $O \in \mathcal{A}$. An observable, O, in $\mathcal{A}$ is a self adjoint operator, i.e., $O = O^{\dagger}$. The algebra $\mathcal{A}$ should contain the relevant observables of a particular system.

Here, the notion of self adjointness is formal and differs from the same notion relative to operators on Hilbert spaces, which imples the identity between the domain of a *symmetric* [46], also called Hermitian, operator and the domain of its adjoint. By construction, an observable in this formalism is an operator of the type (16), which satisfies (compare to (19)), $O(E) = O^*(E)$ and $O(E, E') = O^*(E', E)$, where the asterisk stands for complex conjugation.

A state ρ on $\mathcal{A}$ is a linear mapping (with respect to the structure of linear space on the algebra) $\rho : \mathcal{A} \longmapsto \mathbb{C}$, such that:

i.) The mapping ρ is positive. This means that for each $O \in \mathcal{A}$, $\rho(O^{\dagger}\, O) \geq 0$.

ii.) The mapping ρ is normalized. This means that if I is the identity in $\mathcal{A}$, then, $\rho(I) = 1$.

iii.) The mapping ρ is continuous with respect to the topology on $\mathcal{A}$ and the usual topology on $\mathbb{C}$.

Just restricting ourselves to states of the kind (24) on the algebras $\mathcal{A}^{\pm}$, there are three different types of states:

i.) *Pure states.* A state is pure if the exists a square integrable function $\psi(E) \in L^2(\mathbb{R}^+)$, $\mathbb{R}^+ \equiv [0, \infty)$, such that

$$\rho(E) = |\psi(E)|^2 , \qquad \rho(E, E') = \psi^*(E)\, \psi(E') . \tag{28}$$

Note that $\rho(E, E) = \rho(E)$.

ii.) *Mixtures.*- Just defined by the relation $\rho(E) = \rho(E, E)$. Note that pure states are a particular case of mixtures. For mixtures we do not need the existence of a square integrable function satisfying (28).

iii.) *Generalized states.*- All the others. These states have been introduced [47] in order to give a precise mathematical definition of the states with diagonal singular. This notion has been introduced by van Hove [48, 49] for systems far from the thermodynamic equilibrium. For the van Hove states, $\rho(E) \neq \rho(E, E)$, which still are regular functions, not generalized ones. Nevertheless, we may introduce in this group states for which $\rho(E)$ and $\rho(E, E)$ are generalized functions. Next, we see that Gamow states belong to this category.

2.3. **Gamow States.** Now, we define the notion of Gamow functional, which appeared for the first time in [50] and, then, in [42]. For the growing Gamow vector associated to the resonance pole $z_R = E_R + i\Gamma/2$, we begin with the generalized function $\delta_{z_R} \otimes \delta_{z_R^*}$ and for the decaying Gamow vector associated to the resonance pole $z_R^* = E_R - i\Gamma/2$, the generalized function $\delta_{z_R^*} \otimes \delta_{z_R}$, which act on the test function $O(E, E')$ as

$$(\delta_{z_R} \otimes \delta_{z_R^*} | O(E, E')) := O(z_R, z_R^*) , \quad (\delta_{z_R^*} \otimes \delta_{z_R} | O(E, E')) := O(z_R^*, z_R) , \tag{29}$$

respectively.

Recall that we have demanded that the functions $O(E, E')$ are analytically continuable independently in both variables. Once we have the generalized function (29), we define the following functional on the algebra $\mathcal{A}^-$:

$$\rho_G := \int_0^\infty dE\, \delta(E - E_R)\, (E^-| + \int_0^\infty dE \int_0^\infty dE'\, \delta_{z_R} \otimes \delta_{z_R^*}\, (EE'^-| , \tag{30}$$

and the following functional on the algebra $\mathcal{A}^+$:

$$\rho_D := \int_0^\infty dE\, \delta(E - E_R)\, (E^+| + \int_0^\infty dE \int_0^\infty dE'\, \delta_{z_R^*} \otimes \delta_{z_R}\, (EE'^+| . \tag{31}$$

Functionals (30) and (31) are, respectively, the *growing and the decaying Gamow functionals or Gamow states.* We need to show that ρ_G is a state on $\mathcal{A}^-$ and ρ_D is a state on $\mathcal{A}^+$. We sketch the proof for ρ_G, the proof for ρ_D being identical.

i.) *Positivity.* We have not given details on the construction of the functions $O(E, E')$, since this requires some mathematical subtleties. These subtleties are important in order to show the positivity of these functionals. In particular,

$$(\rho_G|(O^-)^\dagger\, O^-) = |O(E_R)|^2 + |O(z_R, z_R^*)|^2 \geq 0\,, \tag{32}$$

where the positivity of the last term in the right hand side of (32) come from the mentioned mathematical properties.

ii.) *Normalization.* This means that $(\rho_G|I^-) = 1$. The proof is obvious after (22).

iii.) *Continuity.* It comes from the topological properties of the algebras.

We denote the action of a state $\rho^\pm$ on an observable $O^\pm \in \mathcal{A}^\pm$ as $(\rho^\pm|O^\pm)$. Then, the action of ρ_G on $O^- \in \mathcal{A}^-$ is $(\rho_G|O^-)$ and the action of ρ_D on $(\rho_D|O^+)$.

From the definitions of ρ_G and ρ_D, we see that these lie on the kind of *generalized states*, although they are different from the above mentioned van Hove states.

Next, let us show that it is always possible to define averages of observables on Gamow states. The average of the observable $O^\pm$ on the state $\rho^\pm$ should be defined, as usual as the action of $\rho^\pm$ on $O^\pm$, as above. This definition is valid for all observables in $\mathcal{A}^\pm$ (respectively), so that is valid for a wide range of observables. In particular, the averages of the identities in $\mathcal{A}^\pm$ are both one. We also may obtain the averages of the powers of the Hamiltonian using the spectral decomposition (14). They are as may be directly checked from (14,30,31):

$$(\rho_G|H^n) = (\rho_D|H^n) = E_R^n\,. \tag{33}$$

This result coincides with that one given in [35] for $n = 1$, where no average for $n > 1$ can be defined. Thus, we go beyond other attempts in the same direction. This result in (33) seems more reasonable than other proposals [33, 34].

2.3.1. *On the Time Evolution.* First of all, let us go back to equations (30) and (31) defining the Gamow functionals. Both are the sum of two contributions, so that we may split ρ_G and ρ_D as the sum of these terms as:

$$\rho_D = \rho_{DR} + \rho_{DS}\,, \qquad \rho_G = \rho_{GR} + \rho_{GS}\,. \tag{34}$$

In both cases, the first term in this decomposition is called the regular part and the second one the singular part. This terminology is purely conventional.

In order to study the time evolution of Gamow states, we need first to define the time evolution on the algebras $\mathcal{A}^\pm$. This is nothing else than the Heisenberg time evolution for observables. This is given by

$$e^{itH}\, O^\pm\, e^{-itH} = \int_0^\infty dE\, O(E)\, e^{itH}\; |E^\pm\rangle\langle E^\pm|\, e^{-itH}$$

$$+\int_0^\infty dE\int_0^\infty dE'\,O(E,E')\,e^{itH}\,|E^\pm\rangle\langle E'^\pm|\,e^{-itH}$$

$$=\int_0^\infty dE\,O(E)\,|E^\pm\rangle\langle E^\pm|+\int_0^\infty dE\int_0^\infty dE'\,O(E,E')\,e^{it(E-E')}\,|E^\pm\rangle\langle E'^\pm|\,. \quad (35)$$

The Schrödinger evolution of the states is related to the Heisenberg evolution of observables through a well known duality formula, given by the first identity in (36).

$$(e^{-itH}\,\rho_G\,e^{itH}|O^-)=(\rho_G|e^{itH}\,O^-\,e^{-itH})=\int_0^\infty dE\,\delta(E-E_R)\,O(E)$$

$$+\int_0^\infty dE\int_0^\infty dE'\,\delta_{z_R}\otimes\delta_{z_R^*}\,O(E,E')\,e^{it(E-E')}=O(E_R)+O(z_R,z_R^*)\,e^{it(z_R-z_R^*)}$$

$$=O(E_R)+O(z_R,z_R^*)\,e^{t\Gamma}=(\rho_{GR}|O^-)+e^{t\Gamma}\,(\rho_{GS}|O^-)\,. \quad (36)$$

Thus, by omitting the arbitrary $O^-\in\mathcal{A}^-$, we obtain the following time decay for the Gamow state:

$$\rho_G(t)=e^{-itH}\,\rho_G\,e^{itH}=\rho_{GR}+e^{t\Gamma}\,\rho_{GS}\,. \quad (37)$$

Analogously,

$$\rho_D(t)=\rho_{DR}+e^{-t\Gamma}\,\rho_{DS}\,. \quad (38)$$

Observe that, while (36) grows for increasingly positive values of time and decreases for increasingly negative values of time, the opposite is true for (38). A choice of $O(E,E')$ using a kind of complex analytic functions called Hardy functions on a half plane [31, 32] implies the validity of (37) for $t<0$ *only* and the validity of (38) for $t>0$ *only*. Thus, the evolution group splits into two distinct semigroups, one for values of t negatives (the growing part) and the other for values of t positives (the decaying part). This point of view postulates the existence of an origin of times for decaying processes [51].

3. Concluding Remarks

Unstable quantum states, usually called quantum scattering resonances, can be split into two parts: one which have exponential decay at all times, starting from an origin $t=0$. The other shows unescapable big deviations of the exponential law for very small, next to $t=0$, and very large values of time. These are hardly observable, so that exponential decay is assumed to be a good approximation for practically all observable values of time. Then, it looks practical to use resonance states which show an exponential decay for all times. Vector states for these exponential

decay states are called Gamow vectors or Gamow states. Different resonances have distinct Gamow states.

The use of Gamow vectors as a representation of Gamow states has been popular since the years 1950'. However, this representation has two problems. One is the difficulty to define averages of observables on Gamow states. The other is the presumption that Gamow states should have non-zero entropy, which looks incompatible with the representation of Gamow state as vectors, as is the case for pure quantum states. It is certainly true that Gamow vectors are not normalizable, but we still need to show that notwithstanding they are not pure states.

We have used an algebraic formulation of observables and states that solves both problems. In one side, averages on Gamow states are well defined for a wide range of observables. In addition it is shown that Gamow states are not pure (neither mixtures, although they are quantum states).

Author Contribution Statements All authors have equally contributed to this paper.

Declaration of Competing Interests The Authors declare no conflict of interests.

Acknowledgement This work was supported by MCIN with funding from the European Union NextGenerationEU (PRTRC17.I1) and the Consejería de Educación through QCAYLE project, as well as the PID2020-113406GB-I0 project by MCIN of Spain.

References

[1] Bohm, A. Quantum Mechanics: Foundations and Applications, 3rd Ed. Springer Verlag, New York and Berlin, 2001.

[2] Newton, R.G. Scattering Theory of Waves and Particles, 2rd Ed. Springer Verlag, Berlin and Heidelberg, 1982.

[3] Nussenzveig, H.M. Causality and Dispersion Relations, Academic, New York and London, 1972.

[4] Kukulin, V.I.; Krasnopolski, V.M.; Horáček, Theory of Resonances, Principles and Applications, Academia, Prag, 1989.

[5] Fonda, L.; Ghirardi, G.C.; Rimini, A . Decay theory of unstable quantum systems. *Rep Progr. Phys.*, 41 (1978), 587-631, https://doi.org/10.1088/0034-4885/41/4/003.

[6] Khalfin, L.A., Contribution to the decay theory of a quasi stationary state, *Sov. Phys., JETP-USSR* 6 (6) (1958), 1053-1063.

[7] Fischer, M.C.; Gutiérrez-Medina, B.; Raizen, M.G., Observation of the quantum Zeno and anti-Zeno effects in an unstable system, *Phys. Rev. Lett.*, 87 (4) (2001), 040402, https://doi.org/10.1103/PhysRevLett.87.040402.

[8] Rothe, C.; Hintschich, S.I.; Monkman, A.P., Violation of the Exponential-Decay Law at Long Times, *Phys. Rev. Lett.*, 96 (16) (2006), 163601, https://doi.org/10.1103/PhysRevLett.96.163601.

[9] Nakanishi, N., A note on the physical state of unstable particles, *Progr. Theor. Phys.*, 21 (1) (1959), 216-217, https://doi.org/10.1143/PTP.21.216 .
[10] Albeverio, S., Kurasov, P., *Singular Perturbations of Differential Operators*, Lecture Note Series, vol. 271, Cambridge, UK, London Mathematical society.
[11] Losada, M., Fortín, S., Gadella, M. Holik, F., Dynamics of algebras in quantum unstable systems, *Int. J. Mod. Phys. A*, 33 (18-19) 2018, 1850109, https://doi.org/10.1142/S0217751X18501099.
[12] Gelfand, I.M., Shilov, G.E., Generalized Functions, Vol. II, Academic Press, New York, 1964.
[13] Horváth, J., Topological Vector Spaces and Distributions, Addison-Wesley, London, 1966.
[14] Bohm, A., Rigged Hilbert space and the mathematical description of physical systems, Boulder Lecture Notes in Theoretical Physics, Vol. 9A, Gordon and Breach Science Publishers, New York, 1967, 255-317.
[15] Bohm, A., The Rigged Hilbert Space and Quantum Mechanics, Lecture Notes in Physics **78**, Springer, New York, 1978.
[16] Roberts, J.E., Rigged Hilbert spaces in quantum mechanics, *Commun. Math. Phys.*, 2 (1966), 98-119, https://doi.org/10.1007/BF01645448.
[17] Antoine, J.P. Dirac formalism and symmetry problems in quantum mechanics. I. General Dirac formalism. *J. Math. Phys.*, 10 (1969), 53-69, https://doi.org/10.1063/1.1664761.
[18] Melsheimer, O. Rigged Hilbert space formalism as an extended mathematical formalism for quantum systems. I. General theory. *J. Math. Phys.*, 15 (1973), 902-916, https://doi.org/10.1063/1.1666769.
[19] Bellomonte, G.; Trapani, C. Rigged Hilbert spaces and contractive families of Hilbert spaces. *Monatshefte Math.* 164 (2011), 271-285, https://doi.org/10.1007/s00605-010-0249-1.
[20] Bellomonte, G.; di Bella, S.; Trapani, C. Operators in rigged Hilbert spaces: some spectral properties. *J. Math. Anal. Appl.*, 411 (2014), 931-946, https://doi.org/10.1016/j.jmaa.2013.10.025.
[21] Chiba, H. A spectral theory of linear operators on rigged Hilbert spaces under analyticity conditions. *Adv. Math.*, 273 (2015), 324-379, https://doi.org/10.1016/j.aim.2015.01.001.
[22] Chiba, H. A spectral theory of linear operators on rigged Hilbert spaces under analyticity conditions II: Applications to Schrödinger operators. *Kyushu J. Math.*, 72 (2018), 375-405, https://doi.org/10.2206/kyushujm.72.375.
[23] Gadella, M.; Gómez, F. A unified mathematical formalism for the Dirac formulation of quantum mechanics. *Found. Phys.*, 32 (2002), 815-869, https://doi.org/10.1023/A:1016069311589.
[24] Gadella, M.; Gómez, F. On the mathematical basis of the Dirac formulation of Quantum Mechanics. *Int. J. Theor. Phys.*, 42 (2003), 2225-2254, https://doi.org/10.1023/B:IJTP.0000005956.11617.e9.
[25] Gadella, M.; Gómez-Cubillo, F. Eigenfunction Expansions and Transformation Theory. *Acta Appl. Math.*, 109 (2010), 721-742, https://doi.org/10.1007/s10440-008-9342-z.
[26] Celeghini, E., Gadella, M., del Olmo, M.A., Applications of rigged Hilbert spaces in quantum mechanics and signal processing, *J. Math. Phys.*, 57 (2016), 072105, https://doi.org/10.1063/1.4958725.
[27] Celeghini, E., Gadella, M., del Olmo, M.A., Spherical harmonics and rigged Hilbert spaces, *J. Math. Phys.*, 59 (5) (2018), 053502, https://doi.org/10.1063/1.5026740.
[28] Celeghini, E., Gadella, M., del Olmo, M.A., Zernike functions, rigged Hilbert spaces and potential applications, *J. Math. Phys.*, 60 (2019), 083508, https://doi.org/10.1063/1.5093488.
[29] Celeghini, E., Gadella, M., del Olmo, M.A., Groups, Jacobi Functions and rigged Hilbert spaces, *J. Math. Phys.*, 61 (2020), 033508, https://doi.org/10.1063/1.5138238.
[30] Bohm, A., Resonance poles and Gamow vectors in the rigged Hilbert space formulation of quantum mechanics, *J. Math. Phys.*, 22 (12) (1980), 2813-2823, https://doi.org/10.1063/1.524871.

[31] Bohm, A., Gadella, M., Dirac Kets, Gamow Vectors and Gelfand Triplets, Springer Lecture Notes in Physics, 348. Springer Verlag, Berlin 1989, https://doi.org/10.1007/3-540-51916-5.
[32] Civitarese, O., Gadella, M., Physical and Mathematical Aspects of Gamow States, *Phys. Rep.*, 396 (2004), 41-113, https://doi.org/10.1016/j.physrep.2004.03.00.
[33] Berggren, T., On the use of resonant states in eigenfunction expansions of scattering and reaction amplitudes, *Nucl. Phys. A*, 109 (2) (1968), 265-287, https://doi.org/10.1016/0375-9474(68)90593-9.
[34] Berggren, T., Expectation value of an operator in a resonant state, *Phys. Lett. B*, 373 (1-3) (1996), 1-4, https://doi.org/10.1016/0370-2693(96)00132-3
[35] Civitarese, O., Gadella, M., Id Betan, R., On the mean value of the energy for resonance states, *Nucl. Phys. A*, 660 (1999), 255-266, https://doi.org/10.1016/S0375-9474(99)00405-4.
[36] Civitarese, O., Gadella, M., On the concept of entropy for quantum decaying systems, *Found. Phys.*, 43 (2013), 1275-1294, https://doi.org/10.1007/s10701-013-9746-0.
[37] Civitarese, O., Gadella, M., The definition of entropy for quantum unstable systems: A view-point based on the properties of Gamow states, *Entropy*, 20 (4) (2018), 231, https://doi.org/10.1007/s10701-014-9860-7.
[38] Amrein, W.O., Jauch, J.M., Sinha, K.B., Scattering Theory in Quantum Mechanics. Physical Principles and Mathematical Methods, 917 Bejamin, Reading, Massachusetts, USA, 1977.
[39] Reed, M., Simon, B., Scattering Theory, Academic, New York, 1979.
[40] Gelfand, I.M., Vilenkin, Generalized Functions. Applications of Harmonic Analysis, Academic, New York, 1970.
[41] Maurin, K.it Generalized eigenfunction expansions and unitary representations of topological groups, Polish Scientific Publishers, Warszawa, 1968.
[42] Castagnino, M., Gadella, M., Id Betán, R., Laura, R., Gamow functionals on operator algebras, *J. Phys. A: Math. Gen.* 34 (2001), 10067-10083
[43] Gadella, M., et al., To appear in Entropy.
[44] Segal, I.E., Postulates for General Quantum Mechanics, *Annal. Math.*, 48 (1947), 930-948, https://doi.org/10.2307/1969387.
[45] Brateli, O., Robinson, B., *Operator Algebras and Quantum Statistical Mechanics*, Vol I and II, Springer, New York, 1979.
[46] Reed, M., Simon, B., *Functional Analysis*, Academic Press, New York, 1972.
[47] Antoniou, I.E., Laura, R., Suchanecki, Z, Tasaki, S., Intrinsic irreversibility of quantum systems with diagonal singularity, *Phys. A*, 241 (1997), 737-772, https://doi.org/10.1016/S0378-4371(97)00167-2.
[48] van Hove, L., The approach to equilibrium in quantum statistics, *Physica*, 23 (1957), 441-480, https://doi.org/10.1016/S0031-8914(57)92891-4.
[49] van Hove, L., The ergodic behaviour of quantum many-body systems, *Physica*, 25 (1959), 268-276, https://doi.org/10.1016/S0031-8914(59)93062-9.
[50] Castagnino, M., Gadella, M., Id Betán, R., Laura, R., The Gamow functional, *Phys. Lett. A*, 282 (2001), 245-250, https://doi.org/10.48550/arXiv.quant-ph/0209146.
[51] Bohm, A., Bryant, P.W., Uncu, H., Wickramasekara, S., Schleich, W.P., The beginning of time observed in quantum jumps, *Fort. Phys.*, 65 (6-8) (2017), 1700015, http://dx.doi.org/10.1002/prop.201700015.

INSTRUCTIONS TO CONTRIBUTORS

Communications Faculty of Sciences University of Ankara Series A2-A3: Physical Sciences and Engineering is a single-blind peer reviewed open access journal which has been published since 1948 by Ankara University, accepts original research articles written in English in the fields of Physics, Engineering Physics, Electronics/Computer Engineering, Astronomy and Geophysics. Review articles written by eminent scientists can also be invited by the Editor.

Article-processing charges: The publication costs for Communications Faculty of Sciences University of Ankara Series A2-A3: Physical Sciences and Engineering are covered by the journal, so authors do not need to pay an article-processing and submission charges. The PDF copies of accepted papers are free of charges and can be downloaded from the webside. Hard copies of the paper, if required, are due to be charged for the amount of which is determined by the administration each year.

Submission: All manuscripts should be submitted via our online submission: https://dergipark.org.tr/en/journal/2457/submission/step/manuscript/new Note that only two submissions per author per year will be considered. Once a paper is submitted to our journal, all co-authors need to wait 6 months from the submission date before submitting another paper.

Cover Letter: Manuscripts should be submitted in the PDF form used in the peer-review process together with THE COVER LETTER and the source file (Supporting File). In the cover letter the authors should suggest the most appropriate Area Editor for the manuscript and potential four reviewers with full names, universities and institutional email addresses. Proposed reviewers must be experienced researchers in your area of research and at least two of them should be from different countries. In addition, proposed reviewers must not be co-auhors, advisors, students, etc. of the authors. In the cover letter, the author may enter the name of anyone who he/she would prefer not to review the manuscript, with detailed explanation of the reason. Note that the editorial office may not use these nominations, but this may help to speed up the selection of appropriate reviewers.

Preparing your manuscript: Manuscripts should be typeset using as DOC or LaTex. Authors will submit their manuscript and the cover letter via our submission system. A template of manuscript can be reviewed in https://dergipark.org.tr/tr/download/journal-file/20554 (or can be reviewed in pdf form).

Title Page: The title page should contain the title of the paper, full names of the authors, affiliations addresses and e-mail addresses of all authors. Authors are also required to submit their Open Researcher and Contributor ID (ORCID)'s which can be obtained from http://orcid.org as their URL address in the format http://orcid.org/xxxx-xxxx-xxxx-xxxx. Please indicate the corresponding author.

Abstract and Keywords: The abstract should state briefly the purpose of the research. The length of the Abstract should be between 50 to 5000 characters. At least 3 keywords are required.

Math Formulae: Formulas should be numbered consecutively in the parentheses ( ).

Tables: All tables must have numbers (TABLE 1) consecutively in accordance with their appearance in the text and a legend above the table. Please submit tables as editable text not as images.

Figures: All figures must have numbers (FIGURE 1) consecutively in accordance with their appearance in the text and a caption (not on the figure itself) below the figure. Please submit figures as EPS, PDF, TIFF or JPEG format.

Authors Contribution Statement, Declaration of Competing Interests and Acknowledgements should be given at the end of the article before the references.

References: The following format for the references should be used. Authors are urged to use the Communication.csl style (https://dergipark.org.tr/en/download/journal-file/18514) in Mendeley Desktop or Zotero automated bibliography. If manual entry is prefered for bibliography, then all citations must be listed in the references part and vice versa. Below, It has no relationship with the text, but can be used to show sample citations such as; for articles [1, 4], for books/booklets/theses [3], and for proceedings/conferences etc. [2].

[1] Demirci, E., Unal, A., Özalp, N., A fractional order SEIR model with density dependent death rate, Hacettepe J. Math. Stat., 40 (2) (2011), 287–295.

[2] Gairola, A. R., Deepmala, Mishra, L. N., Rate of approximation by finite iterates of q-Durrmeyer operators, Proc. Natl. Acad. Sci. India Sect. A Phys. Sci., 86 (2) (2016), 229–234.

[3] Lehmann, E. L., Casella, G., Theory of Point Estimation, Springer, New York, 2003.

[4] Özalp, N., Demirci, E., A fractional order SEIR model with vertical transmission, Math. Comput. Model., 54 (1-2) (2011), 1–6, https://dx.doi.org/10.1016/j.mcm.2010.12.051.

Peer-review policy: The Editor may seek the advice of two, or three referees, depending on the response of the referees, chosen in consultation with appropriate members of the Editorial Board, from among experts in the field of specialization of the paper. The reviewing process is conducted in strict confidence and the identity of a referee is not disclosed to the authors at any point since we use a single-blind peer review process.

Declarations/Ethics With the submission of the manuscript authors declare that:

- All authors of the submitted research paper have directly participated in the planning, execution, or analysis of study;
- All authors of the paper have read and approved the final version submitted;
- The contents of the manuscript have not been submitted, copyrighted or published elsewhere and the visual-graphical materials such as photograph, drawing, picture, and document within the article do not have any copyright issue;
- The contents of the manuscript will not be copyrighted, submitted, or published elsewhere, while acceptance by the Journal is under consideration.
- The article is clean in terms of 'plagiarism', and the legal and ethical responsibility of the article belong to the author(s). Author(s) also accept that the manuscript may go through plagiarism check using IThenticate software;
- The objectivity and transparency in research, and the principles of ethical and professional conduct have been followed. Authors have also declared that they have no potential conflict of interest (financial or non-financial), and their research does not involve any human participants and/or animals.

Archiving: Research papers published in Communications Faculty of Sciences University of Ankara are archived in the Library of Ankara University (Volume 1-63) and Dergipark immediately following publication with no embargo.

Editor in Chief
Commun. Fac. Sci. Univ. Ank. Ser. A2-A3.
Ankara University, Faculty of Sciences
06100 Beşevler, ANKARA – TURKEY

C O M M U N I C A T I O N S

FACULTY OF SCIENCES
UNIVERSITY OF ANKARA

DE LA FACULTE DES SCIENCES
DE L'UNIVERSITE D'ANKARA

Series A2-A3: Physical Sciences and Engineering

Volume 64 **Number : 1** **Year : 2022**

Research Articles

Review Articles